Disequilibrium REE compositions of garnet and zircon in migmatites reflecting different growth timings during single metamorphism (Aoyama area, Ryoke belt, Japan)

Tetsuo KAWAKAMI[1,*], Kenji HORIE[2,3,4], Tomokazu HOKADA[2,3], Kentaro HATTORI[1], Takafumi HIRATA[1,†]

[1] Department of Geology and Mineralogy, Graduate School of Science, Kyoto University, Kitashirakawa-Oiwake-cho, Sakyo-ku, Kyoto 606-8502, Japan.

[2] National Institute of Polar Research, 10-3 Midori-cho, Tachikawa, Tokyo 190-8518, Japan.

[3] Department of Polar Science, SOKENDAI (The Graduate University for Advanced Studies), 10-3 Midori-cho, Tachikawa, Tokyo 190-8518, Japan.

[4] Research and Development Center for Ocean Drilling Science, JAMSTEC, 2-15 Natsuhsima-cho, Yokosuka, Kanagawa, 237-0061, Japan

* Corresponding author, e-mail: t-kawakami@kueps.kyoto-u.ac.jp

[†]Present address: Geochemical Research Center, Graduate School of Science, The University of Tokyo, 7-3-1 Hongo, Bunkyo-ku, Tokyo 113-0033, Japan

Abstract

Chemical disequilibrium of coexisting garnet and zircon in pelitic migmatites (Aoyama area, Ryoke belt, SW Japan) is shown by microtextural evidences and their heavy rare earth element (HREE) patterns. In zircon, two stages of metamorphic rim growth is observed under cathodoluminescence image, although their SHRIMP U-Pb zircon ages are similar at ca. 92 Ma. Inner and outer rims of zircon tend to show steep HREE patterns irrespective of the U-Pb age. The inner rims tend to give higher U content than the outer rims; some rim analyses give various Th/U ratios of 0.02-0.07 compared to the very low (< 0.02) values seen in the rest of rim analyses. The higher-Th/U values are ascribed to the mixed analyses between thin prograde domains and thick retrograde overgrowths. Zircon grains with inclusions similar to previously-reported melt inclusions are further enclosed in garnet, supporting the growth of thin zircon domains coexisting with garnet during the prograde metamorphism.

Garnet rims are commonly replaced by biotite-plagioclase intergrowths, indicating a back reaction with partial melts. Garnet exhibits decrease in HREE and Y concentrations towards the rim, pointing to its prograde growth. The garnet cores have prograde xenotime inclusions, show steep HREE patterns, and yield growth temperature of ~530-570 ^{o}C by a YAG-xenotime thermometer. On the other hand, the garnet rims have no xenotime inclusion and show flat HREE patterns. Rare garnet domains including sillimanite needles also show flat HREE patterns and low Y concentrations, which

is interpreted as a product of dehydration melting consuming biotite and sillimanite at near-peak *P*-*T* conditions (~800 °C and ~0.5 GPa). One such garnet domain gives nearly-equilibrium REE distribution pattern when paired with the matrix zircon rims.

Retrograde xenotime is present in the cracks in garnet and in the biotite-plagioclase intergrowths, suggesting that retrograde breakdown of garnet released HREE and Y to form it. Considering the availability of HREE and Zr and presence of melt inclusions in zircon rims, most part of the zircon rims with positive HREE patterns likely grew during the melt crystallization stage, meaning that the zircon rims and presently-preserved garnet domains did not grow in equilibrium. The above scenario was tested by the array plot analysis and it gave a result consistent with microtextural and traditional REE distribution constraints. Combination of microtextural and the array plot analyses may become a powerful tool to reliably correlate the zircon ages to the *P*-*T* evolution of the high-grade metamorphic rocks.

Keywords: Rare earth elements, garnet, zircon, high-temperature metamorphism, partial melting.

1. Introduction

Zircon is known to grow in various stages of metamorphism, from prograde to retrograde, especially under the presence of melt (Rubatto et al. 2001; Harley and Kelly, 2007; Imayama et al., 2012; Kohn, 2016). Using the difference in various zircon growth stages, it is possible to estimate the duration of high-temperature metamorphism from zircon alone (e.g., Rubatto et al., 2013; Korhonen et al., 2013), and this becomes more reliable once metamorphic processes such as pressure-temperature (*P-T*) path, partial melting, and zircon growths are correlated petrologically and geochemically (e.g., Rubatto et al., 2013). Partitioning of rare earth elements (REE) between garnet and zircon [D_{REE}(Zrn/Grt)] (Rubatto, 2002; Whitehouse and Platt, 2003; Hokada and Harley, 2004; Kelly and Harley, 2005; Buick et al., 2006; Rubatto and Hermann, 2007; Taylor et al., 2015; 2016) is often used to interpret the equilibrium coexistence between these two phases, and to correlate the zircon ages to garnet-forming metamorphic stages. The array plot that describes REE partitioning between zircon and garnet using D_{Yb}(Zrn/Grt) and D_{Yb}(Zrn/Grt)/D_{Gd}(Zrn/Grt) as the defining features of the relationship (Taylor et al., 2017) provides far more sensitivity to mineral reactions and diffusional processes compared to the traditional REE plots, and enables more detailed interpretation of metamorphic history of the sample (Taylor et al., 2017). This includes ability to show disequilibrium patterns even in the case where the traditional REE plot suggests D_{REE}(Zrn/Grt) equilibrium, and judgement of whether the available data suggests zircon and garnet domains were approaching equilibrium or not (Taylor et al., 2017). Although further experimental data is required to evaluate the importance of the array plot (Taylor et al., 2017), another way to do so is to check the consistency with the interpretation evidenced by firm microtextural constraints in natural examples.

In this study, we constrained the relative timing of garnet and zircon growths during the low-*P/T* type Ryoke metamorphism through detailed analyses of microtextures and the systematic changes in REE patterns of zircon and garnet in two anatectic migmatite samples from the Aoyama area (Ryoke belt, SW Japan) (Fig. 1). The Aoyama area was selected because petrological studies (Kawakami, 2001a; 2002) and geochronological studies on zircon (Kawakami et al., 2013) and monazite (Kawakami and Suzuki, 2011) are already available as a basis of this study. In the studied samples, REE patterns of garnet change from steep HREE patterns to flat ones whereas zircon always shows steep HREE patterns. New petrological and geochemical dataset is used to show different growth timings of zircon and garnet during a single metamorphism that resulted in disequilibrium REE patterns recorded in these two phases. The array plot is applied to this example in order to test whether it consistently evaluates the microstructurally-supported disequilibrium relationship between garnet and zircon, and to further provide a successful example of array plot application to natural examples. Mineral abbreviations are after Kretz (1983).

2. Geological setting

The Ryoke belt is an elongated Cretaceous plutono-metamorphic belt that extends over 800 km in SW Japan (Fig. 1a) where syn- to post-tectonic granitoids and high-*T*, low-*P* type metamorphic rocks are widely exposed (Miyashiro, 1961; Okudaira et al., 1993; Nakajima, 1994; Okudaira, 1996; Ikeda, 1998a, b; Kawakami, 2001a; 2004; Suzuki and Adachi, 1998; Skrzypek et al., 2016, 2018; Takatsuka et al., 2018a, 2018b). The metamorphic rocks are mainly composed of metapelite, metapsammite and metachert of accretionary complex origin. The metamorphic grade generally increases toward the south and the highest-grade metamorphic zone reached granulite facies grade (e.g., Ikeda, 2002) resulting in the formation of migmatites (Brown, 1998; Kawakami, 2001a; 2004; Kawakami and Ikeda, 2003).

The Aoyama area is one of the best-studied areas in the Ryoke belt, where high-grade metasedimentary rocks are widely exposed (Yoshizawa et al., 1966; Hayama et al., 1982; Takahashi and Nishioka, 1994; Kawakami, 2001a; 2001b; Kawakami and Nishioka, 2012) (Fig. 1b). The main rock facies is pelitic-psammitic schists in the northern half, whereas anatectic migmatites is dominant in the southern half (Fig. 1b). Migmatites are mostly metatexite, but diatexite is also common in the southwestern part of the area (Kawakami, 2001a). This area has been divided into two regional metamorphic zones; (i) Sil-Kfs zone where Ms + Qtz is unstable and Sil + Kfs + Bt is stable, and (ii) Grt-Crd zone where Grt + Crd + Bt + Kfs ± Sil is stable (Kawakami, 2001a). The peak *P*-*T* conditions are estimated at 0.30-0.40 GPa and 615-670 $^{\circ}$C for the Sil-Kfs zone, and at 0.45-0.60 GPa and 650-800 $^{\circ}$C for the Grt-Crd zone (Kawakami, 2001a). In the Grt-Crd zone where migmatites are distributed, dehydration melting reaction

$$\mathrm{Bt + Sil + Qtz = Grt + Crd \pm Kfs \pm Ilm + melt} \quad (1)$$

is considered to be responsible for the formation of migmatites (Kawakami, 2001a; 2001b). Finding of the magmatic andalusite from the low-*T* part of the Grt-Crd zone led Kawakami (2002) to propose post-peak, nearly isothermal decompression *P*-*T* path. The electron microprobe dating of monazite from the Grt-Crd zone migmatites gave 96.5 ± 1.9 Ma, interpreted as a timing of prograde monazite growth during the Ryoke regional metamorphism (Kawakami and Suzuki, 2011). Zircon in migmatites develops rims with low Th/U that give U-Pb concordia age of 90.3 ± 2.2 Ma (Kawakami et al., 2013). Presence of melt inclusions (glass and nanogranite) in rims of zircon from migmatite samples suggests that zircon rims grew in the presence of anatectic melts (Kawakami et al., 2013). The duration of regional metamorphism higher than the amphibolite facies grade was estimated at ca. 6 Myr, based on the CHIME monazite and the U-Pb zircon ages mentioned above (Kawakami et al., 2013).

Two post tectonic granitoids, the Kabuto granodiorite and the Ao granite, intrude discordantly to the foliation of metamorphic rocks (Yoshida et al., 1995; Fig. 1b). The Kabuto granodiorite accompanies a contact aureole, and gives a Rb-Sr-whole-rock age of 79.2 ± 10.2 Ma (Tainosho et al., 1999). The Ao granite gives the chemical Th-U-total Pb isochron method (CHIME) monazite age of 79.8 ± 3.9 Ma (Kawakami and Suzuki, 2011). Monazite from the Grt-Crd zone migmatites widely records 83.5 ± 2.4 Ma age, which is interpreted as an age of contact metamorphism by the Ao granite, in addition to the 96.5 ± 1.9 Ma regional metamorphic age (Kawakami and Suzuki, 2011). The 83.5 ± 2.4 Ma age is not recorded in zircon rims, and only recorded in monazite (Kawakami and Suzuki, 2011; Kawakami et al., 2013).

3. Analytical methods

Mineral composition analyses, CL observations, and X-ray elemental mapping of thin section samples Y43 and Y46 (Fig. 1) were performed by JEOL8105 at Department of Geology and Mineralogy, Kyoto University. Analytical conditions for quantitative analyses are 15 kV acceleration voltage, 10 nA beam current, and 3 μm spot size. Natural and synthetic minerals were used as standards and ZAF correction was applied. Conditions for X-ray elemental mapping are 600 nA beam current, focused beam to 1 μm spot size with a dwell time of 15 to 50 milliseconds. The CL observation of zircon grains in thin section samples were performed using panchromatic CL detector (Hamamatsu Photonics Co.) mounted on the JEOL8105.

In situ LA-ICPMS analysis of garnet, biotite and zircon grains under thin section was performed using iCAP-Qc + NWR femtosecond laser (ESI) at Department of Geology and Mineralogy, Kyoto University. Laser pit size was 10 μm for determination of REE pattern of zircon, and was 40 μm for REE analyses of garnet and biotite. Analytical conditions are summarized in Higashino et al. (2015). In the normalization calculation of REE, CI chondrite value of McDonough and Sun (1995) is used.

Samples used for the SHRIMP analysis of zircon were crushed into 1-2 cm sized blocks, and further disaggregated into mineral grains using SELFRAG Lab at Japan Agency for Marine-Earth Science and Technology (JAMSTEC), Yokosuka, Japan. After panning, magnetic separation and heavy liquid separation at JAMSTEC, zircon grains were hand-picked at National Institute of Polar Research (NIPR). Separated zircon grains were observed using low-vacuum SEM (JEOL JSM-5900LV) without any coating prior to the SHRIMP analysis, and then mounted on epoxy resin disc with standard materials at NIPR. After curing, these discs were polished to reveal the internal parts of the mounted grains. The SEM and CL observations of zircon grains were done at NIPR in order to investigate the internal structures of zircon grains. Prior to analysis, the surface of the grain mount was washed with 2% HCl to remove any lead contamination, and then gold-coated (ca. 130A˚). The procedures for Pb and U isotopic analyses of zircon follow Horie et al. (2013) and references therein. Analytical conditions are summarized in Table S1. Absence of correlation between the U-Pb ages and U-contents in zircon suggests that the age variation is not caused by matrix effect (cf. Skrzypek et al., 2016). The SHRIMP analysis of zircon grains, including U-Pb age dating and REE and Ti concentration analyses were done at NIPR. After SHRIMP analyses, the grain mounts were coated with carbon and true color CL images were taken by Gatan ChromaCL2 installed with a field emission SEM (FE-SEM; JEOL JSM-7100F) at NIPR. The electron beam current was about 3 nA at an acceleration voltage of 5 kV.

4. Sample and mineral description

The studied samples are two metatexite migmatites from the high-temperature (*T*) part of the Grt-Crd zone (Fig. 1b). Both samples (Y43 and Y46) mainly consist of garnet, biotite, cordierite, K-feldspar, plagioclase, quartz, and retrograde muscovite (Figs. 2-7). Relic sillimanite is included in cordierite in both samples. In sample Y46, sillimanite is also present in the matrix, and included in plagioclase and garnet (Fig. 2a). These microtextures are consistent with the progress of reaction (1) during prograde to peak metamorphic stage. Whole-rock Zr content of migmatites in the Aoyama area is reported to be ~206-365 ppm. Whole-rock composition of pelitic schists and metatexite migmatites show flat HREE patterns, whereas that of inhomogeneous diatexites varies from flat to decreasing HREE patterns (Kawakami and Kobayashi, 2006).

4.1. Garnet

Garnet porphyroblasts ($Alm_{66-73}Prp_{11-19}Grs_{2-5}Sps_{8-20}$) are generally xenomorphic and rims are significantly replaced by laths of biotite intergrown with plagioclase (termed 'biotite-plagioclase intergrowth' hereafter; Figs. 2-7). Garnet includes plagioclase, biotite, quartz, apatite, prograde xenotime, monazite and zircon (Figs. 2-7). X-ray elemental mapping and line analysis of garnet grains revealed that Fe, Mg and Mn preserve flat pattern at the core and increase of Mn and decrease of Mg at the rim, possibly affected by high-*T* homogenization through diffusion and by retrograde re-equilibrium. In contrast, Ca preserves prograde zoning, although low in concentration. It shows decreasing trend towards the rim, and rarely, higher-Ca annulus is also preserved (Figs. 3, 6). The Ca-zoning is not correlated with presence or absence of apatite inclusions; apatite is both included in higher-Ca and lower-Ca domains (Figs. 2, 6). Concentration of Y in garnet is higher in the core, and is correlated positively with Ca zoning and negatively with P zoning (Figs. 3, 4, 6).

In most of the garnet grains from sample Y46, xenotime is exclusively included in the Y-rich cores (termed 'prograde xenotime' hereafter), and not included in the rims (Figs. 2-4). In sample Y43, prograde xenotime is not found in garnet (Figs. 6, 7). On the other hand, secondary xenotime is present in the cracks in garnet and in the breakdown microtexture of garnet into biotite + plagioclase in both samples (termed 'retrograde xenotime' hereafter; Figs. 2-4, 6). The area of biotite + plagioclase intergrowth where retrograde xenotime is distributed is several times larger than the size of presently-preserved garnet, likely mimicking the outline of original garnet. The cores of the original garnet can be identified based both on the highest Y concentration and presence of prograde xenotime inclusions in garnet, and are in most cases different from the geometric cores of the presently-observed, xenomorphic garnet (Figs. 2-7). The REE patterns of the high-Y cores of the garnet in which prograde xenotime is included show high-HREE concentrations and steep HREE patterns (Figs. 2-4). In garnet rims, HREE concentrations are low compared to the cores. The HREE patterns become flat in the garnet rims where prograde xenotime inclusion is absent (Figs. 2-4). These observations suggest that growth of xenotime and garnet during the prograde metamorphism both contributed in depletion of the bulk Y content of the sample as a whole.

A garnet grain named ‘Grt-4’ in sample Y46 is the only grain that includes sillimanite and lacks prograde xenotime inclusion (Fig. 5). It is xenomorphic in shape and chemically homogeneous in terms of major divalent cations (Fe, Mn, Mg and Ca). X-ray elemental mapping shows development of a thin domain with lower P concentration compared to the rest of the garnet grain (right hand side of Fig. 5c). This domain is free of sillimanite inclusion and predates resorption of the garnet grain because the P zoning is discordantly cut by the xenomorphic outline of the garnet. The HREE concentration of the entire grain is low compared to the prograde xenotime-bearing cores of other garnet grains (Figs. 2-5). The zoning in Y is still preserved in this garnet and decreases from point 4-1 to point 4-7 (Fig. 5). This zoning profile suggests that the point 4-1 corresponds to the core side and the point 4-7 to the rim side of original garnet before resorption, judging from the zoning systematics observed in other garnet grains in the same sample (Figs. 2-4). Because the variation of HREE contents from point 4-2 to point 4-6 is small, the sillimanite-bearing part of the garnet is interpreted to have homogeneous HREE contents. Sillimanite-bearing mode of occurrence (Fig. 5a, e) suggests that this part grew during the near-peak metamorphic stage through the reaction (1), and that almost flat to slightly decreasing HREE patterns from point 4-2 to point 4-6 (Fig. 5g) probably represent the typical HREE pattern of garnet that grew at near-peak metamorphic conditions of the study area. Absence of sillimanite-bearing domains in other garnet grains may be attributed to the significant retrograde replacement of sillimanite-bearing rims through back reaction with partial melts, as suggested by the development of thick biotite-plagioclase intergrowths surrounding garnet (Figs. 2-5).

4.2. Feldspars

Plagioclase occurs as inclusion minerals in Y-rich garnet cores and as matrix minerals. The anorthite content of plagioclase inclusions in the garnet is higher compared to the matrix ones in sample Y46 (Fig. 2a). A plagioclase inclusion in the garnet rim shows similar composition with plagioclase replacing garnet in sample Y43 (Fig. 7a). Plagioclase and K-feldspar in the matrix show rimward increase of P concentration (Fig. 3b).

4.3. Zircon

Zircon is present in the matrix or included in biotite in both samples. Rare zircon inclusion in garnet is finer-grained than the matrix ones. The large grain size of separated zircon grains utilized in SHRIMP analysis (>100 μm long) suggests that most of them were derived from the matrix or were contained as inclusions in biotite. Zircon has metamorphic rim overgrowths developed on detrital cores of various ages. Some grains represent single stage rims, but most grains have inner rims and CL-bright outer rims (Figs. 8, 9). Between the inner rims and the cores are the CL-dark annulus (Figs. 8, 9; Kawakami et al., 2013), which is enriched in Al, Ca, Y and U. The micrometer-size inclusions, found throughout the rims of zircon grains, are similar to earlier reported melt inclusions (Kawakami et al., 2013). They are enriched in K, Al and Si, with lower concentration of Na and Ca, consistent with the melt composition. Therefore, the growth of zircon rims took place under hypersolidus *P-T* conditions as in the case of Kawakami et al. (2013). The dark-CL annulus and μm-sized inclusions in it are found not only from the matrix zircon but also in the zircon grains included in garnet (Fig. 7f). This garnet does not include prograde xenotime (Fig. 7d).

The U-Pb SHRIMP ages were determined for zircon from samples Y43 (33 grains) and Y46 (42 grains). The U-Pb age of the inner rims and outer rims are clearly different in some cases (Fig. 9), but in most cases, the age range of them overlaps for both samples (Fig. 10). They can be chemically discriminated using difference in U concentration in the case of sample Y43, although this distinction is not clear in sample Y46 (Fig. 10a). Concordant ages of zircon rims show continuous variation from ca. 94 Ma to ca. 89 Ma for both samples (Figs. 8, 9), even after excluding the mixed analysis between inner and outer rims. The Th/U ratios of the metamorphic rims are low (< 0.09; Fig. 10b), but some of the older-aged inner rims and mixed analyses between inner and outer rims show higher Th/U ratios (Fig. 10b). Based on these observations, the inner and outer rims are considered as a single age population, although it is likely that the inner rims with higher Th/U ratios (Fig. 10b) crystallized earlier than the outer rims. The weighted mean $^{206}Pb/^{238}U$ age of zircon rims showing Th/U ratio lower than 0.02 was calculated using Isoplot 4.15 (Ludwig, 2012). The results were 91.8 ±0.7 Ma (n = 19, MSWD = 0.85) for sample Y43, and 91.5 ±1.0 Ma (n = 10, MSWD = 0.82) for sample Y46.

Detrital cores of the zircon ranges from 125 ±2 Ma to 2767 ±17 Ma ($^{207}Pb/^{206}Pb$ age), and show higher Th/U ratio (> 0.15) than the rims (Table S2). Other peaks for detrital ages are mainly observed at ca. 156-161, 166-178, 188-202, 210-226, 247-258 and 1827-1847 Ma (Table S2). The concordant age as young as 125 ±2 Ma was previously reported from the study area as well (ca. 120 Ma; Kawakami et al., 2013) and thus suggests the protolith age of the migmatites to be early Cretaceous.

The REE and Ti concentrations of zircon rims were determined by SHRIMP on the same analysis points with the U-Pb dating (Table S2). The rims showed low LREE concentrations and steep M-HREE patterns. Average Yb_n/Dy_n was 9.4 and 7.7 for samples Y43 and Y46, respectively (Figs. 8, 9). The M-HREE pattern of zircon rims are not correlated with U-Pb ages in both samples; they are equally steep for ca. 95 Ma to 89 Ma rims (Figs. 8, 9) except for one analysis point (Y43-19.1). Negative Eu anomaly is present (average Eu/Eu* = 0.1), and Ce anomaly is almost absent (average Ce/Ce* = 1) (Figs. 8, 9). Concentration of Ti was 1.30-2.11 ppm for sample Y43 and 1.38-2.21 ppm for sample Y46 (Table S2). The Ti-in-zircon thermometer was not applied because rutile is absent in the samples and a_{TiO2} is difficult to estimate. Correlation between REE concentration and the U-Pb ages is not observed in either sample (Figs. 8, 9).

4.4. Xenotime, apatite and monazite

Prograde xenotime is included in the Y-rich garnet cores (~300 to ~850 ppm Y) as fine grains less than 10 μm in diameter (Figs. 2-4). It is however not included in the Y-poor garnet rims. A rare, resorbed garnet with sillimanite inclusions (Grt-4; Fig. 5) also has no xenotime inclusion, and the sillimanite-bearing domain in it shows lower HREE and Y concentrations compared to the cores of other garnet grains with prograde xenotime inclusions (Figs. 2-4). Retrograde xenotime is present in the intergrowth of plagioclase and biotite replacing garnet. It is also distributed along cracks in garnet that are filled with secondary biotite (Figs. 2-4).

Apatite and monazite occurs in matrix and as inclusion minerals in garnet and in other constituting minerals. Monazite in plagioclase-biotite intergrowths that replaced garnet has Y-richer rims compared to their cores (Figs. 4c, 7c). Apatite in the plagioclase-biotite intergrowth also has higher Y concentration than those included in garnet (Fig. 6c).

5. Discussion

Different growth timings of garnet and zircon in migmatite formation resulting in disequilibrium REE distribution

In sample Y46 the presence of prograde xenotime inclusions in garnet is correlated with high HREE and Y concentration of the host garnet (e.g., Pyle and Spear, 1999). These domains are interpreted as the cores of original garnet (Fig. 11). Application of a YAG-xenotime thermometer (Pyle and Spear, 2000) to the xenotime-bearing garnet cores containing ~300 to ~850 ppm Y yields temperature estimate of ~530－570 ºC for the garnet core growth. Since monazite is abundant in the studied samples and considered to have coexisted with garnet during prograde metamorphism, the decreasing

Y concentration towards the garnet rims indicates the rimward temperature increase, and thus supports the prograde growth of garnet (Figs. 2-6; Pyle and Spear, 1999; Yang and Rivers, 2002). The temperature estimate for the garnet core formation suggests that the reaction (1) is clearly not responsible for the growth of the garnet cores. More importantly, partial melting of pelitic rocks even by water-saturated reactions will not take place under this temperature condition, suggesting that the zircon rims that include melt inclusions cannot be formed contemporaneous with these high HREE and Y cores of garnet. The petrographic constraints discussed above, therefore, do not support chemical equilibrium between garnet cores and the melt-inclusion-bearing zircon rims.

On the other hand, garnet with sillimanite inclusions (Grt-4; Fig. 5) has no prograde xenotime inclusion, and the sillimanite-bearing domains have lower HREE and Y concentrations than the core of other garnet grains having prograde xenotime inclusions (Figs. 2-5). Garnet preserving both the prograde xenotime-bearing cores and sillimanite-bearing domains (rims) within one grain were not found in the studied samples. Rare occurrence of the sillimanite-bearing garnet and common occurrence of the plagioclase + biotite intergrowths replacing the prograde-xenotime-bearing garnet suggests that the sillimanite-bearing garnet domains (rims) were mostly lost through retrograde back reaction between garnet and melt (e.g., Holness et al., 2011; Figs. 3, 6, 7; 11). Therefore, it is likely that the garnet that was stable at peak metamorphism constituted of cores with prograde xenotime inclusions and rims with sillimanite inclusions (Fig. 11). The D_{REE}(Zrn/Grt) patterns between the zircon rims and the sillimanite-bearing domains of Grt-4 (Grt4-2 to Grt4-7) are different from those reported by Rubatto and Hermann (2007) or Taylor et al. (2015), and thus do not represent chemical equilibrium of these pairs (Fig. 12). Because the sillimanite-bearing garnet is likely formed through the reaction (1), disequilibrium between sillimanite-bearing garnet and zircon rims suggests that the zircon rims (except for the part of inner rims as discussed below) did not grow during the near-peak, garnet growth stage through the reaction (1) (Fig. 11). The most likely domain that attained the near-equilibrium between zircon rims in the matrix is the innermost rim of Grt-4 (Grt4-1; Fig. 5), probably corresponds to the boundary between sillimanite-absent and sillimanite-bearing domains. The conventional D_{REE}(Zrn/Grt) pattern between Grt4-1 and the zircon rims give consistent pattern with those reported by Rubatto and Hermann (2007) (Fig. 12). This point is discussed in detail below using array plots.

Occurring between prograde-xenotime-bearing garnet cores and sillimanite-bearing garnet rims is the xenotime- and sillimanite-free mantle of garnet. This mantle is presently preserved as resorbed garnet margins (Y46; Figs. 2-5) or resorbed garnet grains free of xenotime-bearing cores (Y43; Figs. 6-7) in both samples. Absence of prograde xenotime inclusions in the low-Y domains of the garnet that overgrows xenotime-bearing cores (Y46) suggests that the growth of xenotime and garnet contributed in the depletion of the bulk Y content of the sample, resulting in the destabilization of xenotime. The absence of prograde xenotime inclusions can also be ascribed to their consumption during the prograde garnet growth through a continuous reaction (e.g., Pyle and Spear, 1999). This garnet domain was formed presumably by a reaction different from (1) at the temperature between ~530 ºC and that for (1) (Fig. 11). It is likely that partial melting partly took place during the formation of this garnet domain because the melt-inclusion-like microtexture is seen in the rims of zircon enclosed in the garnet domain, and because the hyper-solidus condition is attained near the *P-T* condition for the reaction (1).

As evidenced by thick replacement of garnet by plagioclase + biotite intergrowths accompanied by the retrograde xenotime growths in both samples, it is likely that back reaction between garnet and melt caused release of trace elements contained in garnet and the growth of accessory minerals that acted as sinks of such trace elements (Figs. 2-7, 11). It is likely as well that Zr contained in garnet was also released into the coexisting partial melts, and formed zircon rims during retrograde yet hypersolidus stage (Fig. 11). Cooling and crystallization of the partial melts was important to attain zircon saturation and crystallization in the melt (e.g., Kelsey et al., 2008). Taking into account the importance of zircon growth during melt crystallization stage, and based on the observation that most of the inner rims and all the outer rims of zircon show constant, low Th/U ratio below 0.02 (Fig. 10b), it is likely that these volumetrically large zircon rims were formed during the retrograde, melt crystallization stage. The lowering of U concentration from the inner rims (exclusive of higher Th/U points discussed below) to the outer rims of zircon is consistent with the interpretation that it reflects depletion of U in the melt as zircon crystallized from it.

However, part of the zircon rims might have grown during prograde metamorphism at hypersolidus conditions because zircon grains enclosing inclusions similar to previously-reported melt inclusions are enclosed in the prograde-xenotime-free garnet (Fig. 7d, f). Since the thickness of the rims of zircon enclosed in garnet were too thin for LA-ICPMS dating, the age of inclusion zircon rims was not successfully determined in this study. Possible mechanisms for the prograde zircon growth is the Ostwald-ripening of preexisting zircon consuming fine grains in partial melts (Kawakami et al., 2013; Takatsuka et al., 2018b), or local-scale transfer/stagnation of small volumes of partial melt inducing the zircon growth (e.g., Harley and Nandakumar, 2014). These possible processes for prograde zircon growth may, in either case, result in variations in zircon composition. This is because fine-grained detrital zircons used for the formation of prograde metamorphic rims likely had compositional variation (Kawakami et al., 2013; Takatsuka et al., 2018b), and because variations in local effective bulk composition will be reflected in the composition of crystallizing zircon rims (Harley and Nandakumar, 2014). The variations in Th/U ratio observed for the limited numbers of relatively older-aged inner rims of zircon (indicated by dotted rectangle; Fig. 10b) may reflect such effects. This suggests that the data points that represent inner rims with higher Th/U ratio (Fig. 10b) are either of prograde origin or the mixed analysis between prograde and retrograde zircon rims. The latter case is more likely, because smaller grain size and thin development of rims of zircon inclusions enclosed in garnet suggests that prograde zircon growth was less abundant than the zircon growth during the melt crystallization stage.

Based on these observations and discussions, it is clear that growth timings of garnet and most part of the zircon rims were different in the case of Ryoke metamorphism (Fig. 11) and is possibly the major reason for the chemical disequilibrium between these two phases. Microtextural constraints suggest that the Y-richer monazite rims and apatite in the plagioclase + biotite intergrowths (Figs. 4c, 7c), whose Y was presumably supplied by the breakdown of garnet, were formed contemporaneous with the zircon rims, and thus most of the inner rims and outer rims of zircon show low Th/U ratio (e.g., Rubatto, 2017). This, in turn, means that the Y-poorer cores of monazite grew during the prograde to peak metamorphic stage, which was dated by electron microprobe monazite dating as 96.5 ± 1.9 Ma (Kawakami and Suzuki, 2011). This value is significantly older than the weighted mean $^{206}Pb/^{238}U$ age of zircon rims showing low Th/U ratio (< 0.02) obtained in this study (91.8 ±0.7 Ma for sample Y43 and 91.5 ±1.0 Ma for sample Y46).

Recently, the array plot is proposed as a new method to evaluate REE partitioning between minerals that provides far more sensitivity to mineral reactions and diffusional processes compared to the traditional REE plots (Taylor et al., 2017). It describes REE partitioning between zircon and garnet using D_{Yb}(Zrn/Grt) and D_{Yb}(Zrn/Grt)/D_{Gd}(Zrn/Grt) as the defining features of the relationship. Since the present study provides firm microtextural evidence and conventional D_{REE}(Zrn/Grt) pattern pointing to the disequilibrium relationship between zircon rims and most of the garnet domains (except for Grt4-1), it is a good natural example to test whether the array plot method consistently evaluates the microstructurally supported disequilibrium relationship. Figure 13a is the array plot constructed for selected Zrn/Grt pairs from samples Y43 and Y46. Zircon grains selected are Y46-26.2 and Y43-4.3 as representative of steep HREE patterns, and Y46-9.1, Y46-11.3, Y46-12.1, Y43-27.3 and Y43-19.1 as representative of less steep HREE patterns (Figs. 8 and 9). Because garnet composition is zoned in the studied samples (Figs. 2-7), REE composition of all the garnet domains are paired with the above-listed zircon compositions for each sample and plotted on Fig. 13a. In selecting these pairs we intended to give the largest variation in the array plot. Both Y43 and Y46 data gave an array that does not overlap with strain model results (Fig. 13a), suggesting that these Zrn/Grt pairs are not in equilibrium. However, a pair of Y46-11.3/Grt4-1, that is, (the zircon rim with less steep HREE pattern)/(the innermost rim of the sillimanite-bearing garnet) plot near the strain model data for 700^{o}C (Fig. 13a), suggesting their near-equilibrium relationship. Figure 13b is constructed using pairs of (matrix zircon rims)/(sillimanite-bearing garnet). A few points for zircon/Grt4-1 pairs plot near the strain model result for 700^{o}C, but the rest of them are not consistent with the strain model results. Data points of other garnet domains Grt4-2 and Grt4-7 also plot away from the strain model results (Fig. 13b). These results points to near-equilibrium relationship between the matrix zircon rims and the innermost rim of the sillimanite-bearing garnet, and disequilibrium relationship between the matrix zircon rims and the rest of garnet domains. Such findings are consistent with the interpretation obtained from microtextural and traditional REE plot analyses.

In this study, microstructural analysis played significant role in understanding the prograde/retrograde evolution of the studied samples. The array plot analysis meanwhile played an important role in evaluating the parts of the inner rims of matrix zircon that correspond to the stage of garnet formation through the reaction (1). The array plot also revealed that most of the matrix zircon rims correspond to the melt crystallization stage at the early retrograde metamorphism (Fig. 11). Therefore, our example suggests that combination of microtextural analysis and the array plot analysis may become a powerful tool to reliably correlate the zircon ages to the *P*-*T* evolution of the high-grade metamorphic rocks, and contribute to the detailed understanding of the rates of metamorphic processes.

Acknowledgements

Rich Taylor and anonymous reviewer are thanked for constructive reviews and Marco Scambelluri for editorial handling. Simon Harley is thanked for constructive comments on the previous version of the manuscript. Shuhei Sakata are thanked for technical supports in LA-ICPMS analyses at Kyoto University. Ken-ichiro Tani is thanked for assistance in zircon separation at JAMSTEC. Gabriel Theophilus Valera is thanked for checking English expressions. This study was financially supported by JSPS KAKENHI Grant Number JP26400513 and the General Collaboration Project of the National Institute of Polar Research (No. 25-14) to TK.

References

Brown, M., 1998, Unpairing metamorphic belts: P-T paths and a tectonic model for the Ryoke Belt, southwest Japan. Journal of Metamorphic Geology, 16, 3-22.

Buick, I.S., Hermann, J., Williams, I.S., Gibson, R.L., Rubatto, D., 2006. A SHRIMP U-Pb and LA-ICP-MS trace element study of the petrogenesis of garnet-cordierite-orthoamphibole gneisses from the Central Zone of the Limpopo Belt, South Africa. Lithos 88, 150-172.

Harley, S.L., Kelly, N.M., 2007, Zircon, tiny but timely. Elements 3, 13-18.

Harley, S.L., Nandakumar, V., 2014, Accessory mineral behaviour in granulite migmatites: a case study from the Kerala Khondalite Belt, India. Journal of Petrology, 55, 1965-2002.

Hayama, Y., Yamada, T., Ito, M., Kutsukake, T., Masaoka, K., Miyakawa, K., Mochizuki, Y., Nakai, Y., Tainosho, Y., Yoshida, M., Kawarabayashi, I., Tsumura, Y., 1982. Geology of the Ryoke Belt in the eastern Kinki District, Japan -The phase-divisions and the mutual relations of the granitic rocks-. Journal of the Geological Society of Japan 88, 451-466. (in Japanese with English abstract)

Higashino, F., Kawakami, T., Tsuchiya, N., Satish-Kumar, M., Ishikawa, M., Grantham, G.H., Sakata, S., Hattori, K., Hirata, T. 2015, Geochemical behavior of zirconium during Cl-rich aqueous fluid infiltration under upper amphibolite facies metamorphism – A case study from Brattnipene, Sør Rondane Mountains, East Antarctica. Journal of Mineralogical and Petrological Sciences, 100, 166-178.

Hokada, T., Harley, S.L., 2004. Zircon growth in UHT leucosome: constraints from zircon-garnet rare earth elements (REE) relations in Napier Complex, East Antarctica. Journal of Mineralogical and Petrological Sciences 99, 180-190.

Holness, M.B., Cesare, B., Sawyer, E.W., 2011. Melted Rocks under the microscope: Microstructure and their interpretation. Elements 7, 247–252.

Horie K., Takehara M., Suda Y. and Hidaka H., 2013. Potential Mesozoic reference zircon from Unazuki plutonic complex: geochronological and geochemical characterization. Island Arc 22, 292–305.

Ikeda, T., 1998a. Progressive sequence of reactions of the Ryoke metamorphism in the Yanai district, southwest Japan: the formation of cordierite. Journal of Metamorphic Geology 16, 39-52.

Ikeda, T., 1998b, Phase equilibria and the pressure-temperature path of the highest-grade Ryoke metamorphic rocks in the Yanai district, SW Japan. Contributions to Mineralogy and Petrology 132, 321-335.

Ikeda, T., 2002. Regional occurrence of orthopyroxene-bearing basic rocks in the Yanai district, SW Japan: evidence for granulite-facies Ryoke metamorphism. Island Arc 11, 185-192.

Imayama, T., Takeshita, T., Keewook, Y., Cho, D.-L., Kitajima, K., Tsutsumi, Y., Kayama, M., Nishido, H., Okumura, T., Yagi, K., Itaya, T., and Sano, Y., 2012. Two-stage partial melting and contrasting cooling history within the Higher Himalayan Crystalline Sequence in the far-eastern Nepal

Himalaya. Lithos, 134-135, 1–22.

Kawakami, T., 2001a. Tourmaline breakdown in the migmatite zone of the Ryoke metamorphic belt, SW Japan. Journal of Metamorphic Geology 19, 61-75.

Kawakami, T., 2001b. Boron depletion controlled by the breakdown of tourmaline in the migmatite zone of the Aoyama area, Ryoke metamorphic belt, SW Japan. Canadian Mineralogist 39, 1529-1546.

Kawakami, T., 2002. Magmatic andalusite from the migmatite zone of the Aoyama area, Ryoke metamorphic belt, SW Japan, and its importance in constructing the *P-T* path. Journal of Mineralogical and Petrological Sciences 97, 241-253.

Kawakami, T., 2004. Tourmaline and boron as indicators of the presence, segregation and extraction of melt in pelitic migmatites: examples from the Ryoke metamorphic belt, SW Japan. Transactions of the Royal Society of Edinburgh: Earth Sciences 95, 111-124.

Kawakami, T., Ikeda, T., 2003. Depletion of whole-rock boron controlled by the breakdown of tourmaline and retrograde formation of borosilicates in the Yanai area, Ryoke metamorphic belt, SW Japan. Contributions to Mineralogy and Petrology 145, 131-150.

Kawakami, T., Kobayashi, T., 2006. Trace element composition and the degree of partial melting of pelitic migmatites from the Aoyama area, Ryoke metamorphic belt, SW Japan: Implications for the source region of tourmaline leucogranites. Gondwana Research, 9, 176-188.

Kawakami, T., Nishioka, Y., 2012. Metamorphic rocks and granitoids in the Aoyama area, Ryoke belt, SW Japan. Journal of the Geological Society of Japan 118, Supplement. 79-89. (in Japanese)

Kawakami, T., Suzuki, K., 2011. CHIME monazite dating as a tool to detect polymetamorphism in high temperature metamorphic terrane: Example from the Aoyama area, Ryoke metamorphic belt, Southwest Japan. Island Arc 20, 439-453.

Kawakami, T., Yamaguchi, I., Miyake, A., Shibata, T., Maki, K., Yokoyama, D.T., Hirata, T., 2013. Behavior of zircon in the upper-amphibolite to granulite facies schist/migmatite transition, Ryoke metamorphic belt, SW Japan: constraints from the melt inclusions in zircon. Contributions to Mineralogy and Petrology 165, 575-591.

Kelly, N.M., Harley, S.L., 2005. An integrated microtextural and chemical approach to zircon geochronology: refining the Archaean history of the Napier Complex, east Antarctica. Contributions to Mineralogy and Petrology 149, 57-84.

Kelsey, D. E., Clark, C., Hand, M., 2008. Thermobarometric modelling of zircon and monazite growth in melt-bearing systems: examples using model metapelitic and metapsammitic granulites. Journal of Metamorphic Geology 26, 199-212.

Kohn, M.J., 2016. Metamorphic chronology—a tool for all ages: Past achievements and future prospects. American Mineralogist, 101, 25–42.

Korhonen, F.J., Clark, C., Brown, M., Bhattacharya, S., Taylor, R., 2013. How long-lived is ultrahigh temperature (UHT) metamorphism? Constraints from zircon and monazite geochronology in the Eastern Ghats orogenic belt, India. Precambrian Research 234, 322-350.

Kretz, R., 1983. Symbols for rock-forming minerals. American Mineralogist 68, 277-279.

Ludwig, K.R., 2009. SQUID 2: A User's Manual, rev. 12 Apr, 2009. Berkeley Geochronology Center, Special Publication 5. 110 p.

Ludwig, K.R., 2012. User's manual for Isoplot 3.75. A geological toolkit for Microsoft Excel. Berkeley Geochronology Center Special Publication No.5, revision of January 30, 2012. 75p.

McDonough, W.F., Sun, S.–s., 1995. The composition of the Earth. Chemical Geology 120, 223-253.

Miyashiro, A., 1961. Evolution of metamorphic belts. Journal of Petrology, 2, 277-311.

Nakajima, T., 1994. The Ryoke plutonometamorphic belt: Crustal section of the Cretaceous Eurasian continental margin. Lithos 33, 51-66.

Okudaira, T., 1996. Temperature-time path for the low-pressure Ryoke metamorphism, Japan, based on chemical zoning in garnet. Journal of Metamorphic Geology 14, 427-440.

Okudaira, T., Hara, I., Sakurai, Y., Hayasaka, Y., 1993. Tectono-metamorphic processes of the Ryoke belt in the Iwakuni-Yanai district, southwest Japan. Memoirs of the Geological Society of Japan 42, 91-120.

Ozaki, M., Sangawa, A., Miyazaki, K., Nishioka, Y., Miyachi, Y., Takeuchi, K., Tagutschi, Y., 2000. Geology of the Nara District. With geological sheet map at 1 : 50,000, Geological Survey of Japan,

p. 162 (in Japanese with English abstract p. 5)

Pyle, J.M., Spear, F.S., 1999. Yttrium zoning in garnet: coupling of major and accessory phases during metamorphic reactions. Geological Materials Research 1, 1-49.

Pyle, J.M., Spear, F.S., 2000. An empirical garnet (YAG)－xenotime thermometer. Contributions to Mineralogy and Petrology 138, 51-58.

Rubatto, D., 2002. Zircon trace element geochemistry: partitioning with garnet and the link between U-Pb ages and metamorphism. Chemical Geology 184, 123-138.

Rubatto, D., 2017. Zircon: The metamorphic mineral. Reviews in Mineralogy and Geochemistry, 83, 261–295.

Rubatto, D., Chakraborty, S., Dasgupta, S., 2013. Timescales of crustal melting in the Higher Himalayan Crystallines (Sikkim, Eastern Himalaya) inferred from trace element-constrained monazite and zircon chronology. Contributions to Mineralogy and Petrology 165, 349-372.

Rubatto, D., Hermann, J., 2007. Experimental zircon/melt and zircon/garnet trace element partitioning and implications for the geochronology of crustal rocks. Chemical Geology 241, 38-61.

Rubatto, D., Williams, I.S., Buick, I.S., 2001. Zircon and monazite response to prograde metamorphism in the Reynolds Range, central Australia. Contributions to Mineralogy and Petrology 140, 458-468.

Skrzypek, E., Kato, T., Kawakami, T., Sakata, S., Hattori, K., Hirata, T., Ikeda, T., 2018, Monazite behavior and time-scale of metamorphic processes along a low-pressure/high-temperature field gradient (Ryoke belt, SW Japan). Journal of Petrology, 59, 1109–1144.

Skrzypek, E., Kawakami, T., Hirajima, T., Sakata, S., Hirata, T., Ikeda, T. 2016, Revisiting the high temperature metamorphic field gradient of the Ryoke Belt (SW Japan): new constraints from the Iwakuni-Yanai area. Lithos, 260, 9-27.

Suzuki, K., Adachi, M., 1998. Denudation history of the high T/P Ryoke metamorphic belt, southwest Japan: constraints from CHIME monazite ages of gneisses and granitoids. Journal of Metamorphic Geology 16, 23- 37.

Tainosho, Y., Kagami, H., Yuhara, M., Nakano, S., Tsuda, K., Morioka, K., 1999, High initial Sr isotopic ratios of Cretaceous to Early Paleogene granitic rocks in Kinki district, southwest Japan. The Memoirs of the Geological Society of Japan, 53, 309-321.

Takahashi, Y., Nishioka, Y., 1994. Mode of plagioclase twinnings in Ryoke metamorphic rocks in the western area of Tsu City, Mie Prefecture. Journal of the Japanese Association of Mineralogist, Petrologists and Economic Geologists 89, 261-268. (in Japanese with English abstract)

Takatsuka, K., Kawakami, T., Skrzypek, E., Sakata, S., Obayashi, H., Hirata, T. 2018a, Age gap between the intrusion of gneissose granitoids and regional high-temperature metamorphism in the Ryoke belt (Mikawa area, central Japan). Island Arc, e12224.

Takatsuka, K., Kawakami, T., Skrzypek, E., Sakata, S., Obayashi, H., Hirata, T. 2018b, Spatiotemporal evolution of magmatic pulses and regional metamorphism during a Cretaceous flare-up event: constraints from the Ryoke belt (Mikawa area, central Japan). Lithos, 308-309, 428-445.

Taylor, R.J.M., Clark, C., Harley, S.L., Kylander-Clark, A.R.C., Hacker, B.R., Kinny, P.D., 2017. Interpreting granulite facies events through rare earth element partitioning arrays. Journal of Metamorphic Geology, 35, 759-775.

Taylor, R.J.M., Harley, S.L., Hinton, R.W., Elphick, S., Clark, C., Kelly, N.M., 2015. Experimental determination of REE partition coefficients between zircon, garnet and melt: a key to understanding high-T crustal processes. Journal of Metamorphic Geology, 33, 231-248.

Taylor, R.J.M., Kirkland, C.L., Clark, C., 2016. Accessories after the facts: Constraining the timing, duration and conditions of high-temperature metamorphic processes. Lithos, 264, 239-257.

Whitehouse, M.J., Platt, J.P., 2003, Dating high-grade metamorphism-constraints from rare-earth elements in zircon and garnet. Contributions to Mineralogy and Petrology, 145, 61-74.

Yang, P., Rivers, T., 2002. The origin of Mn and Y annuli in garnet and the thermal dependence of P in garnet and Y in apatite in calcpelite and pelite, Gagnon terrane, western Labrador. Geological Materials Research 4, 1-35.

Yoshida, F., Takahashi, Y., Nishioka, Y., 1995. Geology of the Tsu-Seibu district. With geological sheet map at 1:50,000. Geological Survey of Japan. (in Japanese with English abstract)

Yoshizawa, H., Nakajima, W., Ishizaka, K., 1966. The Ryoke metamorphic zone of the Kinki district, Southwest Japan: Accomplishment of a regional geological map. Memoirs of the College of Science, University of Kyoto, Series B 32, 437-453.

Figure captions

Fig. 1. (a) Simplified geological map of the Ryoke belt. The low-temperature, high-pressure type Sanbagawa belt is located to the south of the Ryoke belt and the two belts are separated by the Median Tectonic Line (MTL). TTL: Tanakura Tectonic Line, ISTL: Itoigawa-Shizuoka Tectonic Line. (b) Geological map of the Aoyama area (after Yoshida et al., 1995; Ozaki et al., 2000) showing the sample localities of Y43 and Y46. The Grt-Crd and tourmaline-out isograds (Kawakami, 2001a; Kawakami et al., 2013) are subparallel to the schist/migmatite boundary and to the penetrative schistosity/migmatitic banding observed in this area.

Fig. 2. X-ray elemental maps and a back-scattered electron image of a garnet porphyroblast in sample Y46 (Grt-1) that are replaced by laths of biotite grains intergrown with plagioclase. (a) X-ray elemental map of Ca. Note that rimward decrease in Ca is preserved in garnet. (b) X-ray elemental map of P. Note the abundant P-bearing inclusion minerals in garnet. (c) X-ray elemental map of Y. Note the prograde xenotime inclusions in the lower-left part of the garnet. (d) BSE image of garnet with distribution of accessory minerals. Black squares numbered 1-1 to 1-9 represent spots for *in situ* LA-ICPMS REE analyses. (e) Trace element zoning of garnet. Points 1-1 to 1-9 correspond to numbers in black squares shown in (d). Orange arrows represent the garnet domain

in which prograde xenotime (Xtm) is included. (f) Chondrite-normalized REE pattern of garnet. Points 1-1 to 1-9 correspond to numbers in black squares shown in (d). Orange bar represents the garnet domain in which prograde xenotime is included. Note that garnet domains with prograde xenotime inclusions show steep HREE patterns.

Fig. 3. X-ray elemental maps and a back-scattered electron image of a garnet porphyroblast in sample Y46 (Grt-2) that are replaced by laths of biotite grains intergrown with plagioclase. (a) X-ray elemental map of Ca. Note that a Ca-rich annulus is preserved in garnet. (b) X-ray elemental map of P, preserving the zoning in P that show negative correlation with the zoning in Ca. (c) X-ray elemental map of Y. Note the prograde xenotime inclusions in the garnet core. (d) BSE image of garnet with distribution of accessory minerals. Black squares numbered 2-1 to 2-8 represent spots for *in situ* LA-ICPMS REE analyses. (e) Trace element zoning of garnet. Points 2-1 to 2-8 correspond to numbers in black squares shown in (d). Orange arrows represent the garnet domain in which prograde xenotime is included. (f) Chondrite-normalized REE pattern of garnet. Points 2-1 to 2-8 correspond to numbers in black squares shown in (d). Orange bar represents the garnet domain in which prograde xenotime is included. Note that garnet domains with prograde xenotime inclusions show steep HREE patterns.

Fig. 4. X-ray elemental maps and a back-scattered electron image of a garnet porphyroblast in sample Y46 (Grt-3) that are replaced by laths of biotite grains intergrown with plagioclase. (a) X-ray

elemental map of Ca. Note that a Ca-rich core is preserved in garnet. (b) X-ray elemental map of P. Note the abundant P-bearing inclusion minerals enclosed in garnet. (c) X-ray elemental map of Y. Note the prograde xenotime inclusions in the Y-rich garnet core. (d) BSE image of garnet with distribution of accessory minerals. Black squares numbered 3-1 to 3-6 represent spots for *in situ* LA-ICPMS REE analyses. (e) Trace element zoning of garnet (ppm). Points 3-1 to 3-6 correspond to numbers in black squares shown in (d). Orange arrows represent the garnet domain in which prograde xenotime is included. (f) Chondrite-normalized REE pattern of garnet. Points 3-1 to 3-6 correspond to numbers in black squares shown in (d). Orange bar represents the garnet domain in which prograde xenotime is included. Note that garnet domains with prograde xenotime inclusions show steep HREE patterns.

Fig. 5. Photomicrograph, X-ray elemental maps and a back-scattered electron image of a garnet porphyroblast in sample Y46 (Grt-4). (a) Photomicrograph of Grt-4. Sillimanite needles are included in most part of the garnet. Open nicol. (b) X-ray elemental map of Ca. (c) X-ray elemental map of P. Note the presence of P-poor rim at the right hand side of the garnet. (d) X-ray elemental map of Y. (e) BSE image of garnet with distribution of accessory minerals. Black squares numbered 4-1 to 4-7 represent spots for *in situ* LA-ICPMS REE analyses. (f) Trace element zoning of garnet (ppm). Points 4-1 to 4-7 correspond to numbers in black squares shown in (e). (g) Chondrite-normalized REE pattern of garnet. Points 4-1 to 4-7 correspond to numbers

in black squares shown in (e).

Fig. 6. X-ray elemental maps and a back-scattered electron image of a garnet porphyroblast in sample Y43 (Grt-1) that are replaced by laths of biotite grains intergrown with plagioclase. (a) X-ray elemental map of Ca. Note that a Ca-rich core and Ca-rich annulus is preserved in garnet. (b) X-ray elemental map of P negatively correlated with the pattern by Ca. (c) X-ray elemental map of Y, positively correlated with the pattern by Ca. (d) BSE image of garnet with distribution of accessory minerals. Black squares numbered 1-1 to 1-6 represent spots for *in situ* LA-ICPMS REE analyses. (e) Trace element zoning of garnet (ppm). Points 1-1 to 1-6 correspond to numbers in black squares shown in (d). (f) Chondrite-normalized REE pattern of garnet. Points 1-1 to 1-6 correspond to numbers in black squares shown in (d).

Fig. 7. X-ray elemental maps and a back-scattered electron image of a garnet porphyroblast in sample Y43 (Grt-2) that are replaced by laths of biotite grains intergrown with plagioclase. (a) X-ray elemental map of Ca. Note that a Ca-rich core is preserved in garnet. (b) X-ray elemental map of P. (c) X-ray elemental map of Y. Note the chemical zoning preserved in monazite grains. (d) BSE image of garnet with distribution of accessory minerals. Black squares numbered 2-1 to 2-8 represent spots for *in situ* LA-ICPMS REE analyses. (e) Trace element zoning of garnet (ppm). Points 2-1 to 2-8 correspond to numbers in black squares shown in (d). (f) Chondrite-normalized REE pattern of garnet. Points 2-1 to 2-8 correspond to numbers in black squares shown in (d).

Inset is CL and BSE images of ‘Zrn 3’ included in garnet. Note that inclusion-rich, CL-dark and BSE-bright annulus is present.

Fig. 8. Results of zircon rim analyses in sample Y43 determined by SHRIMP. (a) Selected chondrite-normalized REE patterns. Insets are the selected CL images of separated zircon grains and SHRIMP ages $\pm 2\sigma$ error. Red ellipsoids represent analysis points. Numbers shown in the top left of each CL-image is the zircon grain number (corresponds to the grain number shown in Tables S1 and S2). (b) Wetherill diagram for all zircon rims analyzed. (c) Probability density plot for all zircon rim ages.

Fig. 9. Results of zircon rim analyses in sample Y46 determined by SHRIMP. (a) Selected chondrite-normalized REE patterns. Insets are selected CL images of separated zircon grains and SHRIMP ages $\pm 2\sigma$ error. Red ellipsoids represent analysis points. Numbers shown in the top left of each CL-image is the zircon grain number (corresponds to the grain number shown in Tables S1 and S2). (b) Wetherill diagram for all zircon rims analyzed. (c) Probability density plot for all zircon rim ages.

Fig. 10. (a) Concordant U-Pb age vs U (ppm) plot for inner and outer rims of zircon from samples Y43 and Y46. (b) Concordant U-Pb age vs Th/U ratio plot for inner and outer rims of zircon from samples Y43 and Y46. Indicated by dotted rectangle are data points with variations in Th/U ratio, ascribed to mixed analyses between prograde and retrograde zircon rims. Error bars for U-Pb age,

U concentration and Th/U ratio are ±2 σ .

Fig. 11. A cartoon showing the deduced microtextural development. See text for details.

Fig. 12. D_{REE}(zircon/garnet) pattern obtained from sample Y46. The REE composition of garnet was determined by *in situ* LA-ICPMS analysis and that of zircon was determined by SHRIMP.

Fig. 13. Array plots for samples Y43 and Y46 that describe REE partitioning between zircon and garnet using D_{Yb}(Zrn/Grt) and D_{Yb}(Zrn/Grt)/D_{Gd}(Zrn/Grt) as the defining features of the relationship (Taylor et al., 2017). (a) Selected zircon/garnet pairs plotted in the figure are (Y46-26.2)/(Grt-2-1 to 8), (Y46-12.1)/(Grt-2-1 to 8), (Y46-26.2)/(Grt-4-1 to 7), (Y46-9.1)/(Grt-4-1 to 7), (Y46-11.3)/(Grt-4-1 to 7), (Y43-4.3)/(Grt1-1 to 6), (Y43-27.3)/(Grt1-1 to 6), (Y43-4.3)/(Grt2-1 to 8), and (Y43-27.3)/(Grt2-1 to 8). Selection of these pairs are intended to give the largest variation in the plot from available REE data of garnet and zircon. (b) Selected zircon/garnet pairs plotted in the figure are (all available zircon from sample Y46)/(Grt4-1, 4-2, 4-7). Note that pairs with Grt4-1 give similar value with a strain model result at 700 ^{o}C.

Table S1. Analytical conditions for U–Pb zircon dating, trace elements (REE, Y, and Nb) including Hf, and Ti content of samples Y43 and Y46 by SHRIMP.

Table S2. Summary of results of the (a)(b) SHRIMP U-Pb dating for samples Y43 and Y46, (c) REE, Y, Nb, and Hf concentration analyses, and (d) Ti concentration analyses. See text and Table S1 for analytical conditions.

Table S3. Summary of REE analyses of garnet grains from samples Y43 and Y46 determined by *in situ* LA-ICPMS analysis.

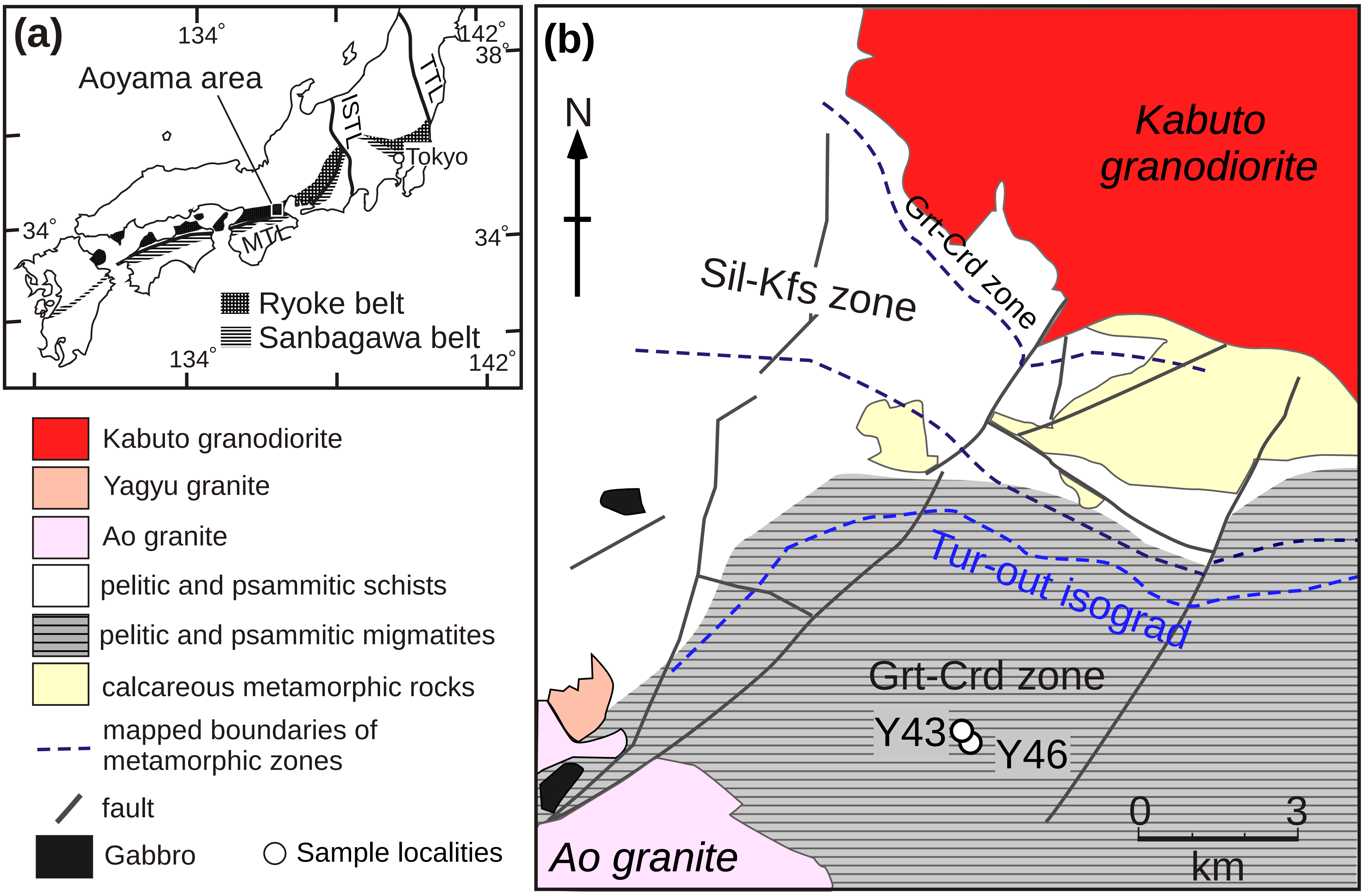

Kawakami et al. Fig. 1

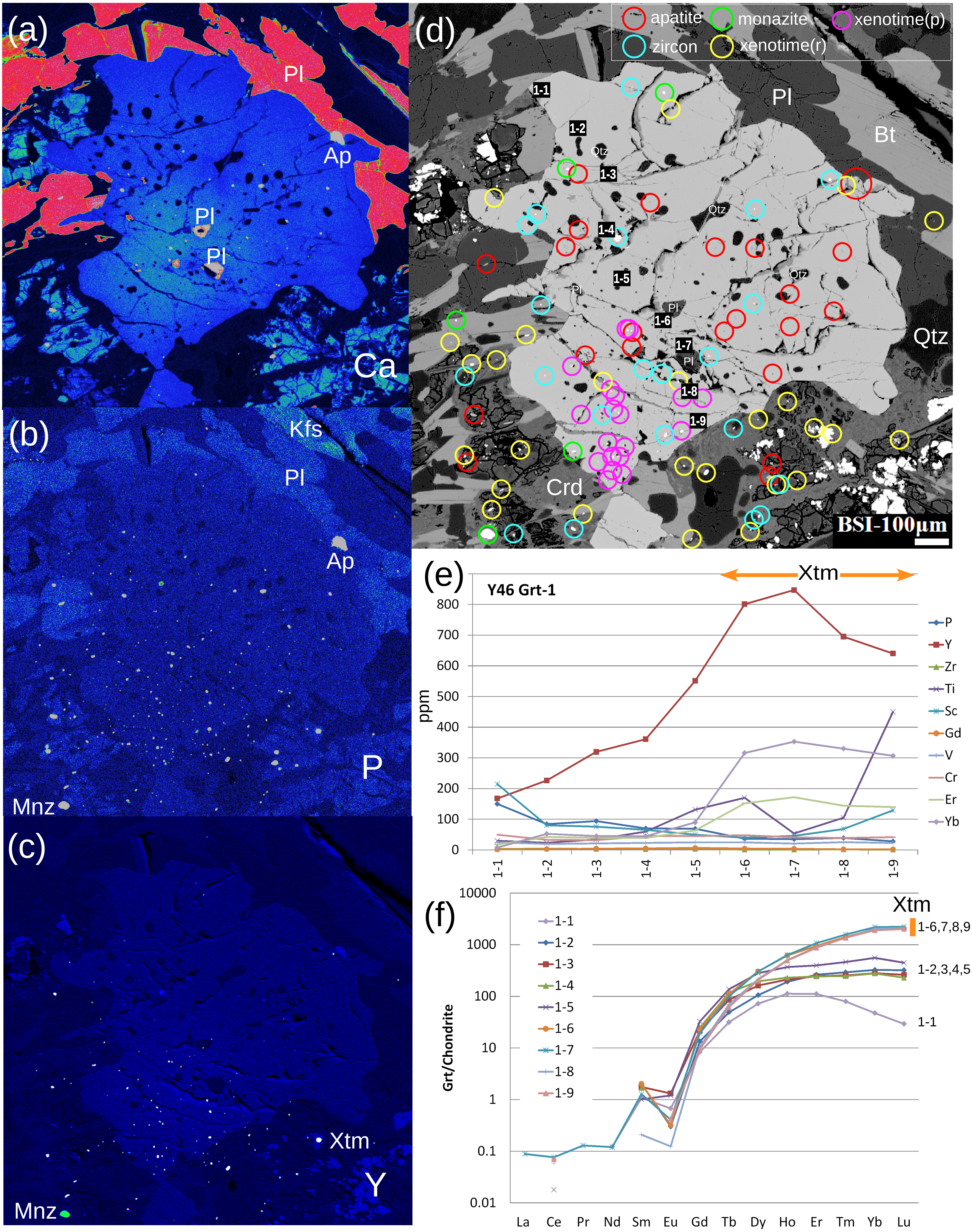

Kawakami et al. Fig. 2

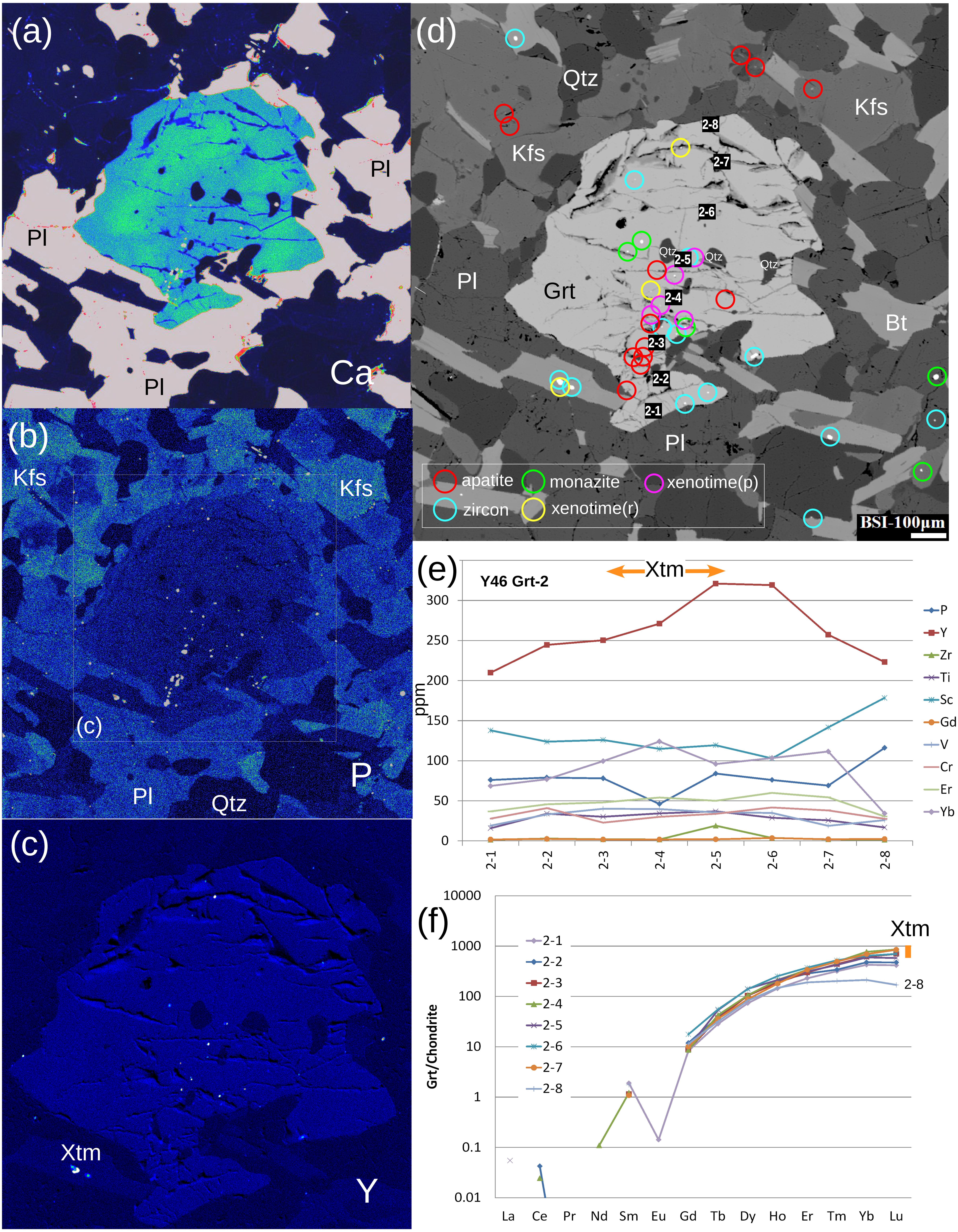

Kawakami et al. Fig. 3

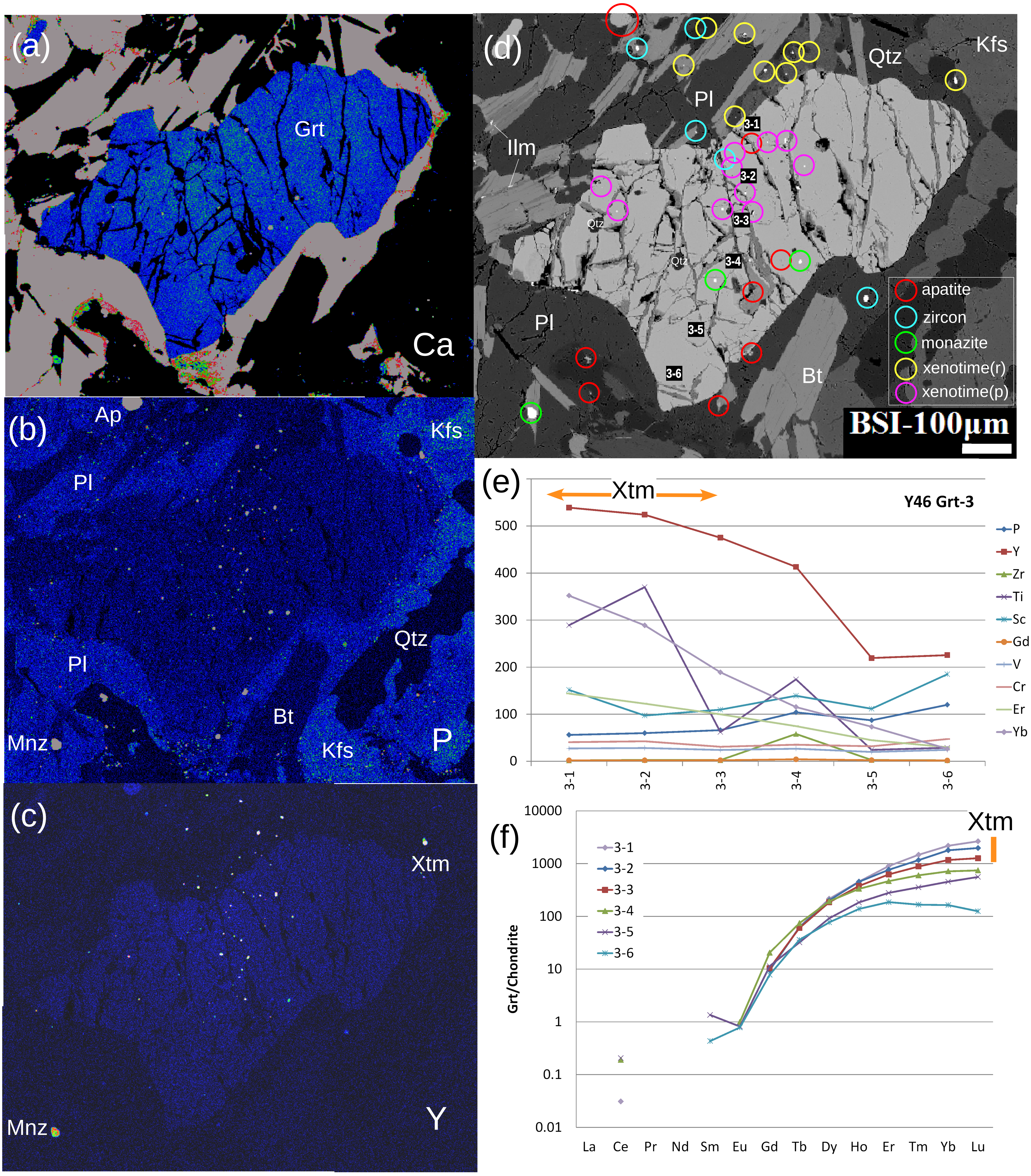

Kawakami et al. Fig. 4

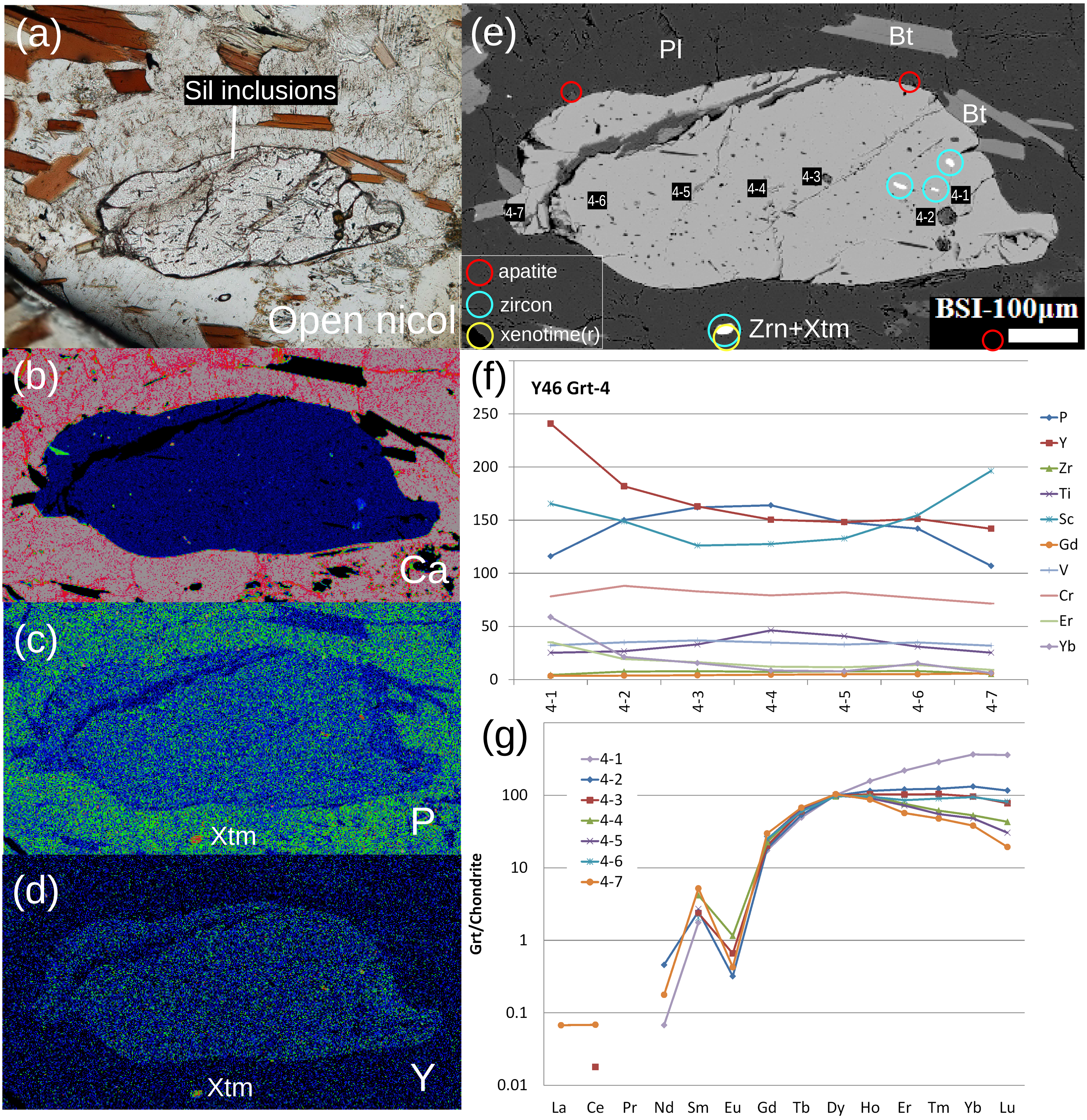

Kawakami et al. Fig. 5

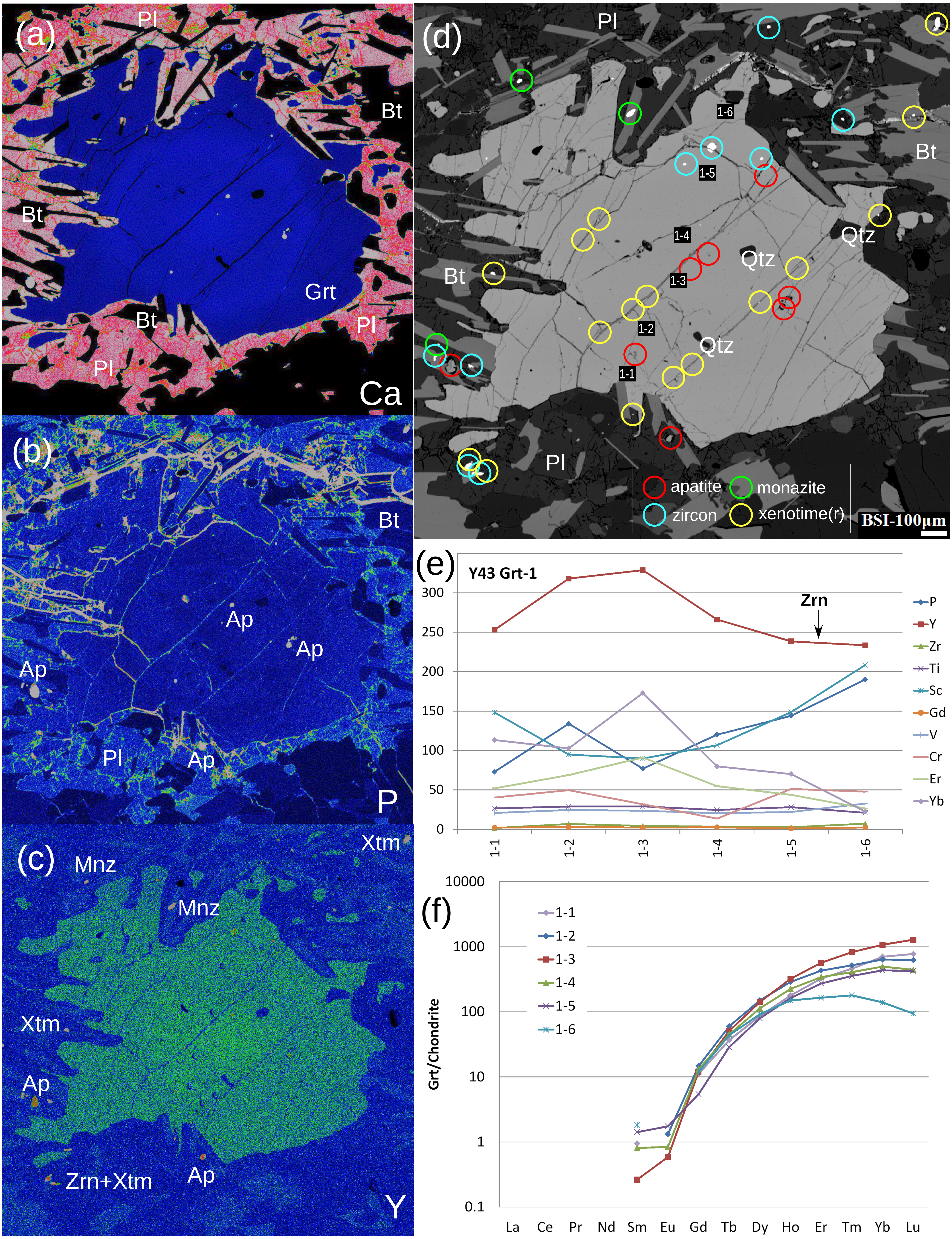

Kawakami et al. Fig. 6

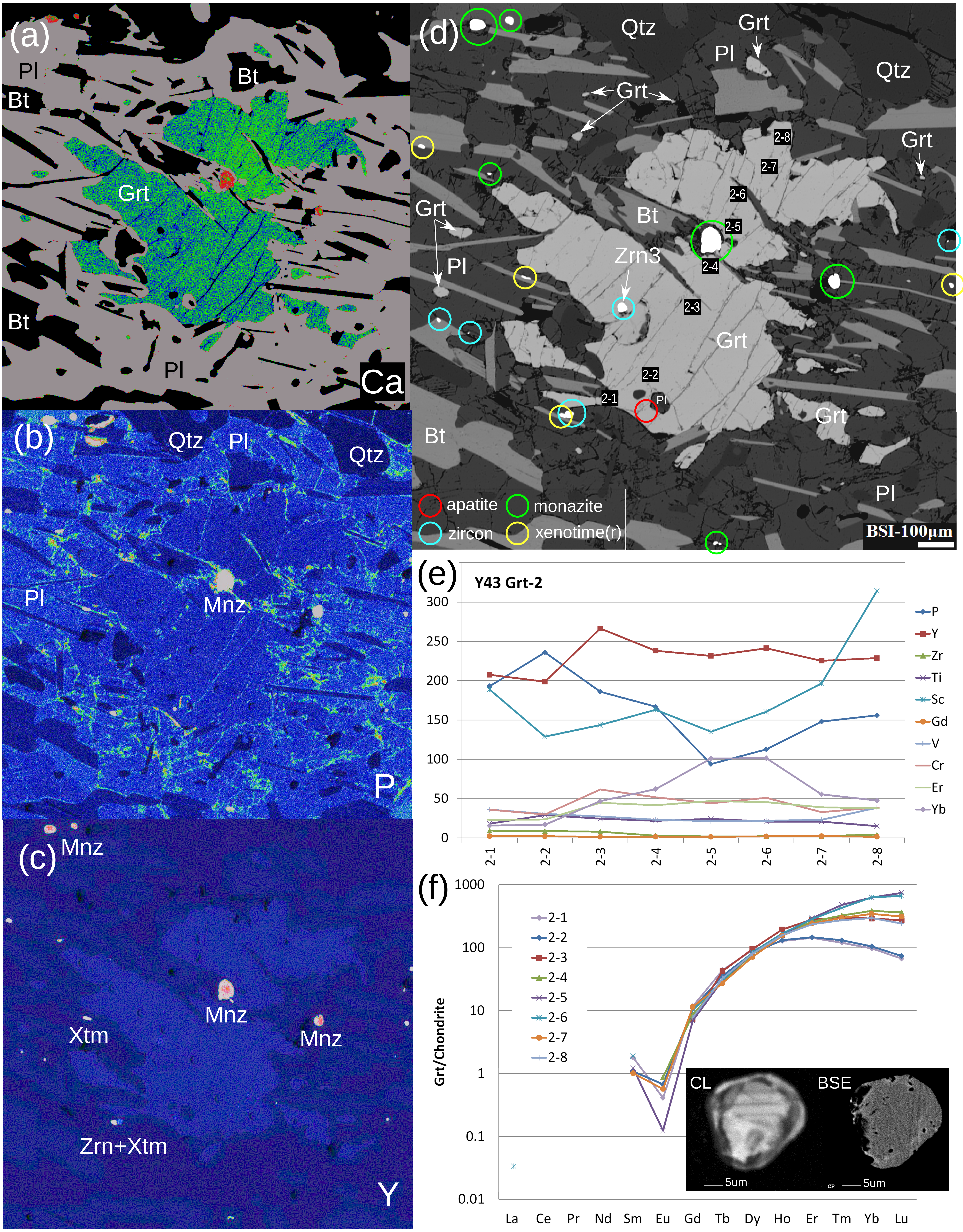

Kawakami et al. Fig. 7

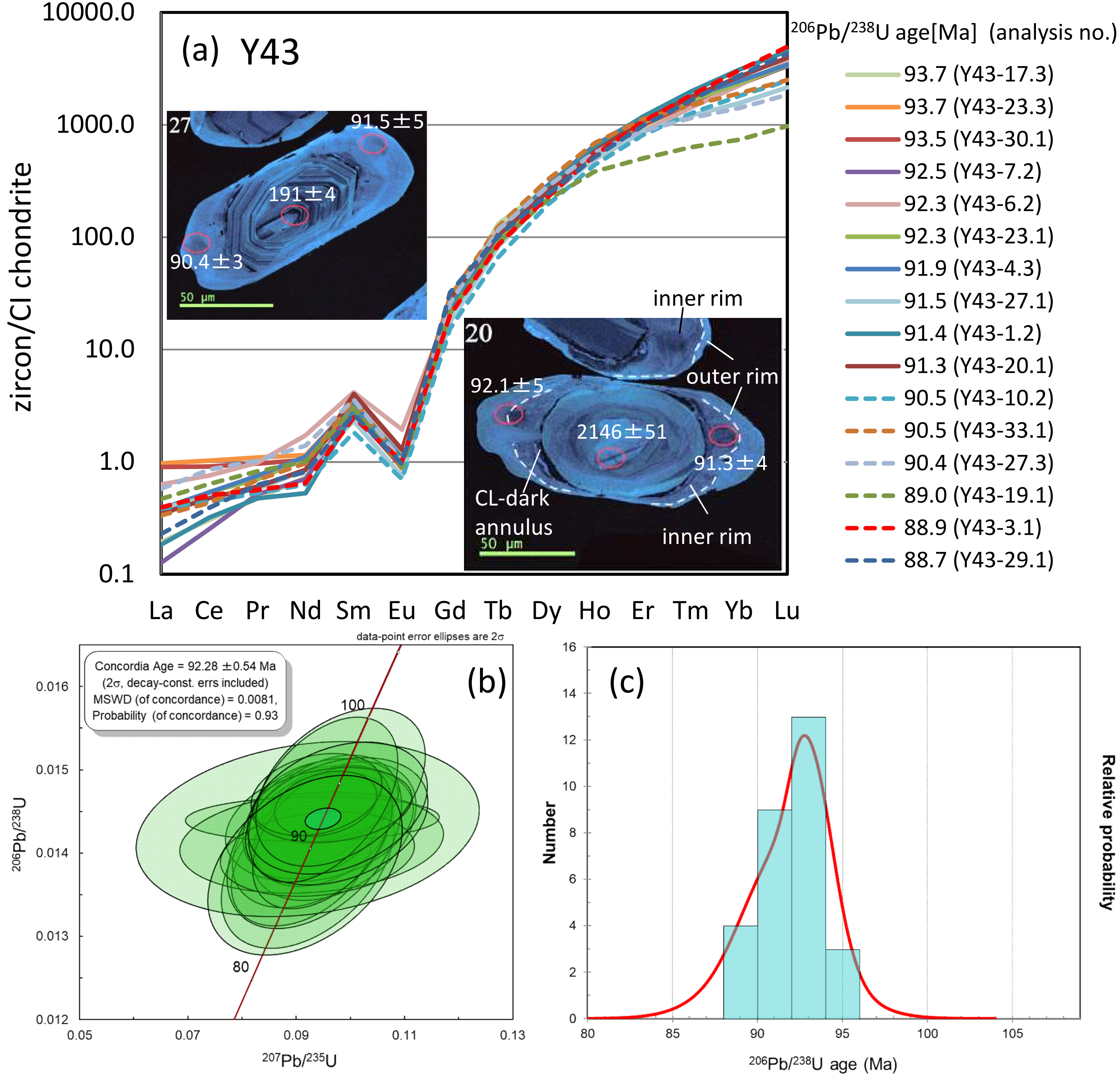
(a) Y43
10000.0
1000.0
100.0
10.0
1.0
0.1
zircon/CI chondrite
La Ce Pr Nd Sm Eu Gd Tb Dy Ho Er Tm Yb Lu
27
91.5±5
191±4
90.4±3
50 μm
20
inner rim
outer rim
92.1±5
2146±51
91.3±4
CL-dark
annulus
inner rim
50 μm
206Pb/238U age[Ma] (analysis no.)
93.7 (Y43-17.3)
93.7 (Y43-23.3)
93.5 (Y43-30.1)
92.5 (Y43-7.2)
92.3 (Y43-6.2)
92.3 (Y43-23.1)
91.9 (Y43-4.3)
91.5 (Y43-27.1)
91.4 (Y43-1.2)
91.3 (Y43-20.1)
90.5 (Y43-10.2)
90.5 (Y43-33.1)
90.4 (Y43-27.3)
89.0 (Y43-19.1)
88.9 (Y43-3.1)
88.7 (Y43-29.1)
data-point error ellipses are 2σ
Concordia Age = 92.28 ±0.54 Ma
(2σ, decay-const. errs included)
MSWD (of concordance) = 0.0081,
Probability (of concordance) = 0.93
(b)
100
90
80
206Pb/238U
0.016
0.015
0.014
0.013
0.012
0.05 0.07 0.09 0.11 0.13
207Pb/235U
(c)
Number
16 14 12 10 8 6 4 2 0
80 85 90 95 100 105
206Pb/238U age (Ma)
Relative probability

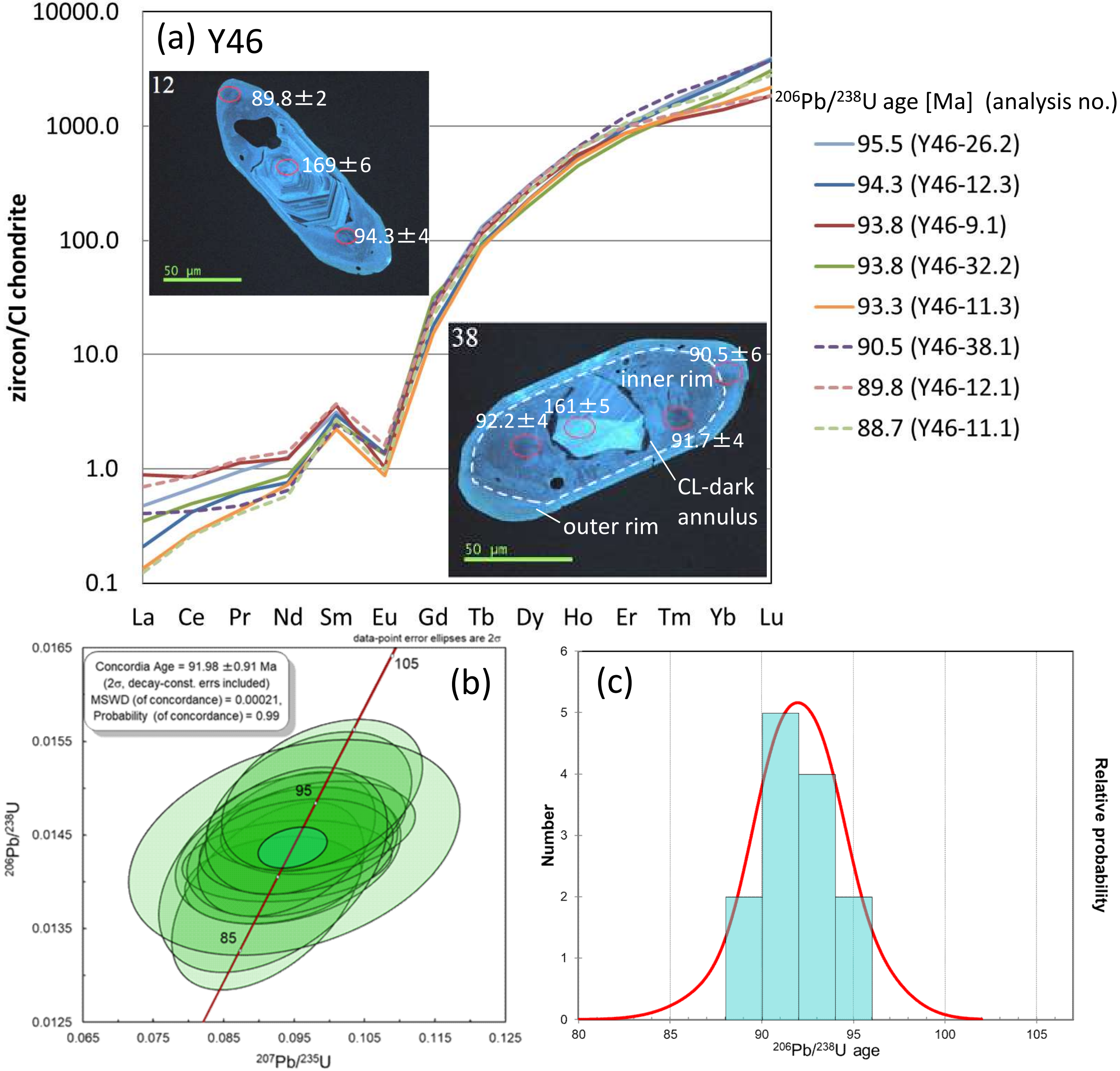

(a) Y46
10000.0
1000.0
100.0
10.0
1.0
0.1
zircon/CI chondrite
La Ce Pr Nd Sm Eu Gd Tb Dy Ho Er Tm Yb Lu
12
89.8±2
169±6
94.3±4
50 μm
38
90.5±6
inner rim
161±5
92.2±4
91.7±4
CL-dark annulus
outer rim
50 μm
206Pb/238U age [Ma] (analysis no.)
95.5 (Y46-26.2)
94.3 (Y46-12.3)
93.8 (Y46-9.1)
93.8 (Y46-32.2)
93.3 (Y46-11.3)
90.5 (Y46-38.1)
89.8 (Y46-12.1)
88.7 (Y46-11.1)
data-point error ellipses are 2σ
Concordia Age = 91.98 ±0.91 Ma
(2σ, decay-const. errs included)
MSWD (of concordance) = 0.00021,
Probability (of concordance) = 0.99
(b)
105
95
85
206Pb/238U
207Pb/235U
0.0165
0.0155
0.0145
0.0135
0.0125
0.065 0.075 0.085 0.095 0.105 0.115 0.125
(c)
Number
Relative probability
206Pb/238U age
80 85 90 95 100 105
0 1 2 3 4 5 6

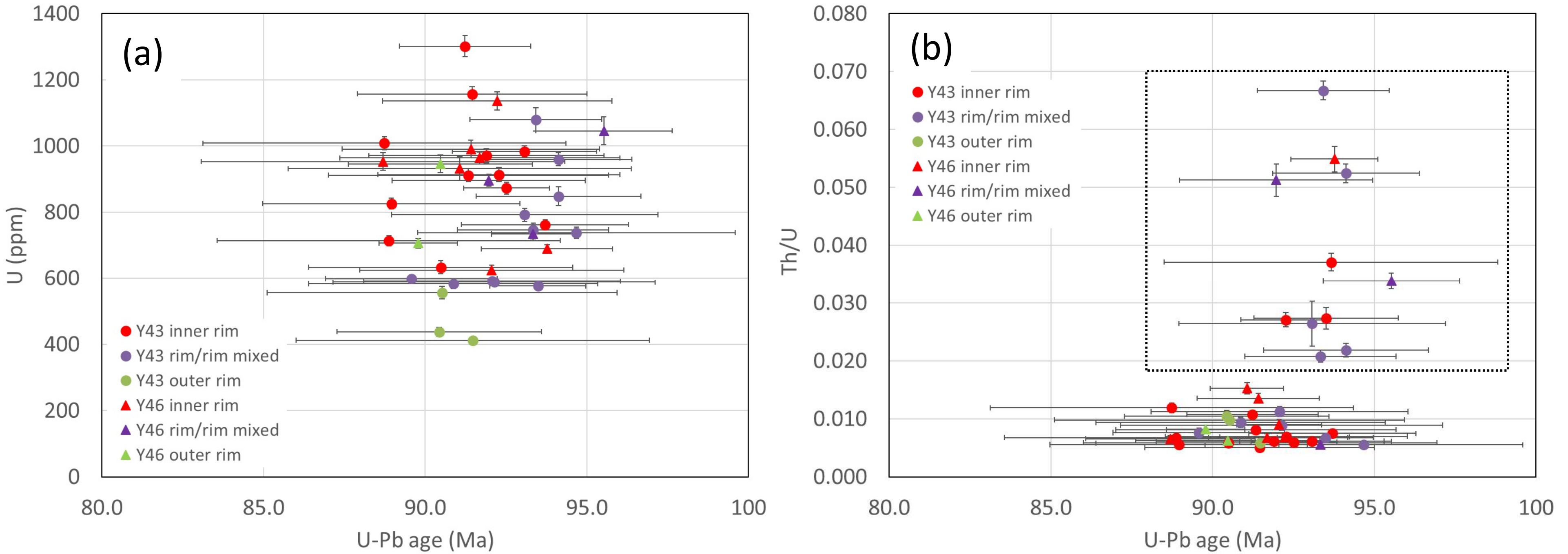
(a)
U (ppm)
1400
1200
1000
800
600
400
200
0
80.0
85.0
90.0
95.0
100
U-Pb age (Ma)
Y43 inner rim
Y43 rim/rim mixed
Y43 outer rim
Y46 inner rim
Y46 rim/rim mixed
Y46 outer rim
(b)
Th/U
0.080
0.070
0.060
0.050
0.040
0.030
0.020
0.010
0.000
80.0
85.0
90.0
95.0
100
U-Pb age (Ma)
Y43 inner rim
Y43 rim/rim mixed
Y43 outer rim
Y46 inner rim
Y46 rim/rim mixed
Y46 outer rim

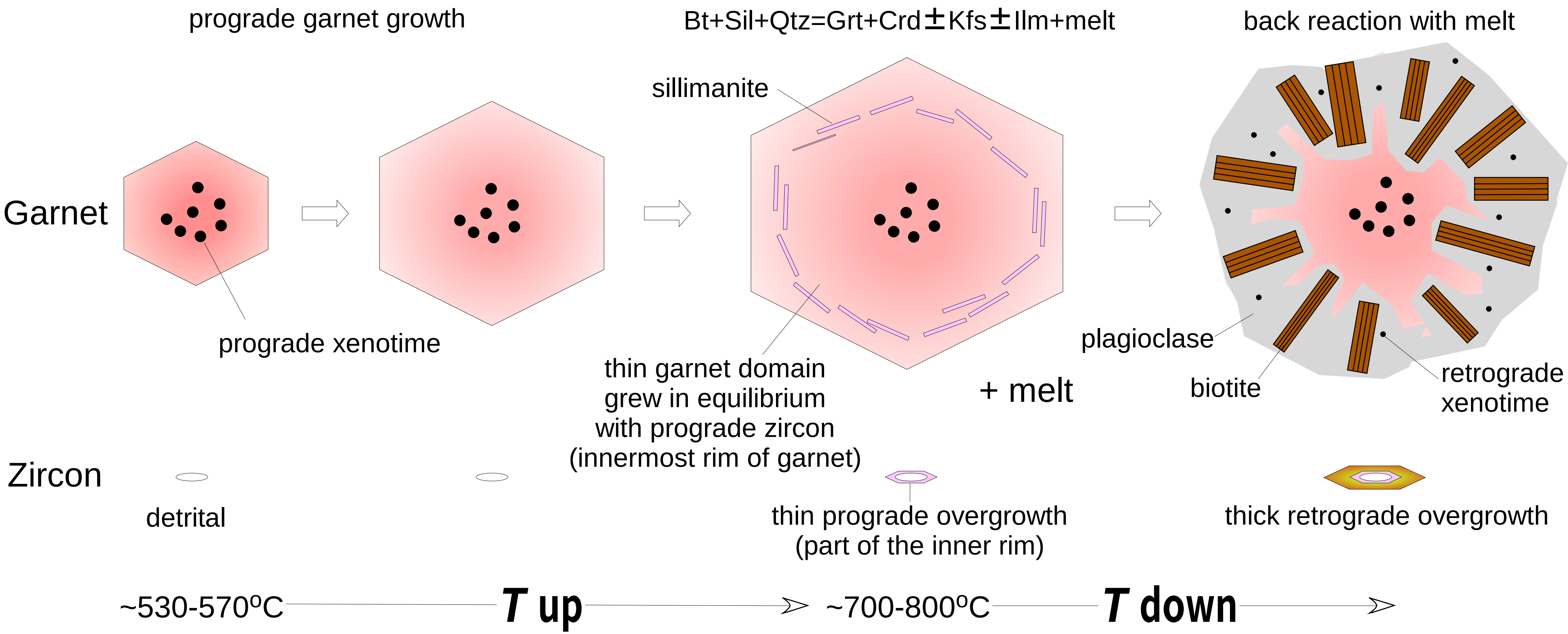

prograde garnet growth
Bt+Sil+Qtz=Grt+Crd±Kfs±Ilm+melt
back reaction with melt
sillimanite
Garnet
prograde xenotime
thin garnet domain
grew in equilibrium
with prograde zircon
(innermost rim of garnet)
+ melt
plagioclase
biotite
retrograde
xenotime
Zircon
detrital
thin prograde overgrowth
(part of the inner rim)
thick retrograde overgrowth
~530-570ºC
T up
~700-800ºC
T down

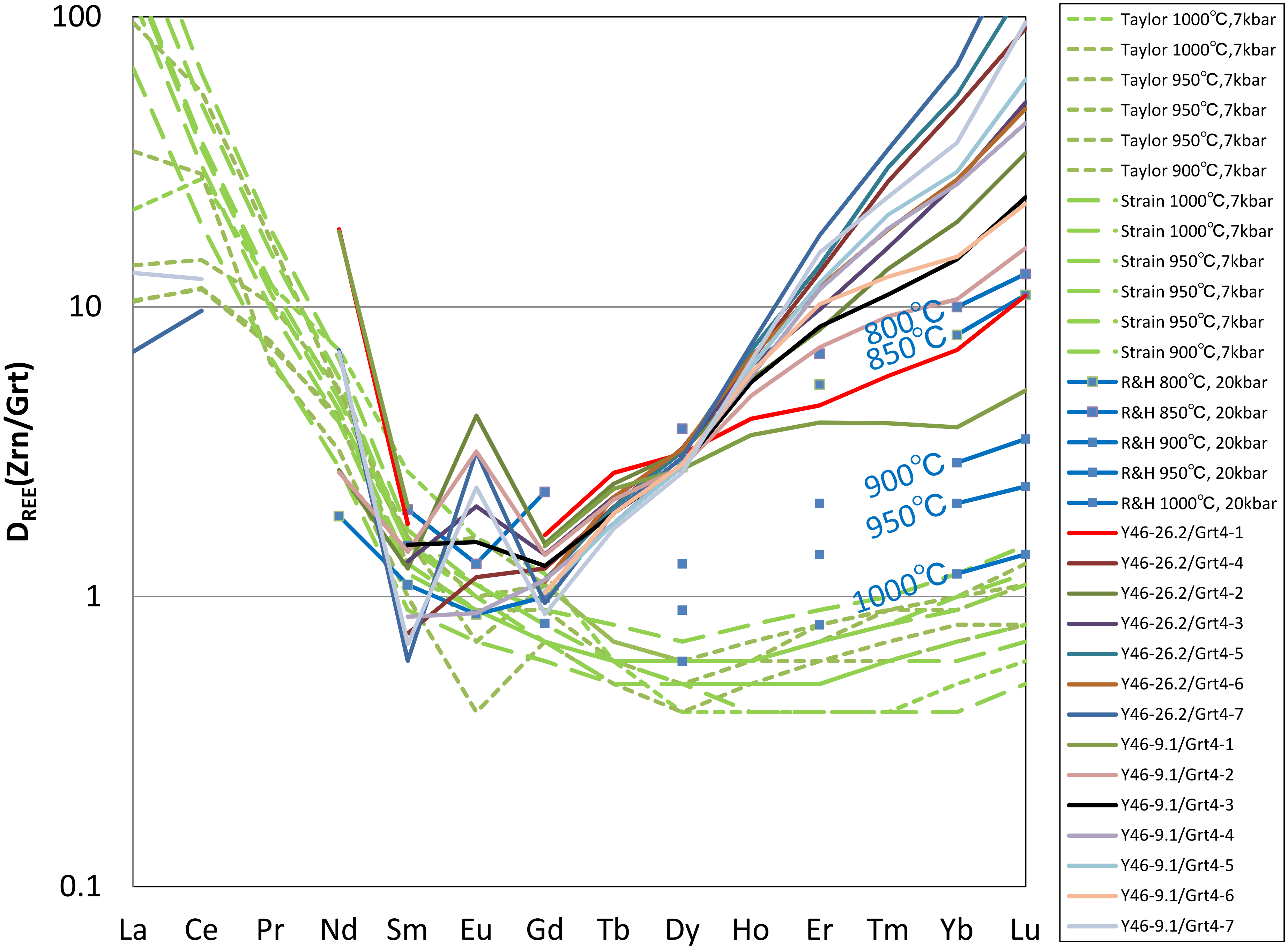

D_REE(Zrn/Grt)
100
10
1
0.1
La
Ce
Pr
Nd
Sm
Eu
Gd
Tb
Dy
Ho
Er
Tm
Yb
Lu
800°C
850°C
900°C
950°C
1000°C
Taylor 1000°C,7kbar
Taylor 1000°C,7kbar
Taylor 950°C,7kbar
Taylor 950°C,7kbar
Taylor 950°C,7kbar
Taylor 900°C,7kbar
Strain 1000°C,7kbar
Strain 1000°C,7kbar
Strain 950°C,7kbar
Strain 950°C,7kbar
Strain 950°C,7kbar
Strain 900°C,7kbar
R&H 800°C, 20kbar
R&H 850°C, 20kbar
R&H 900°C, 20kbar
R&H 950°C, 20kbar
R&H 1000°C, 20kbar
Y46-26.2/Grt4-1
Y46-26.2/Grt4-4
Y46-26.2/Grt4-2
Y46-26.2/Grt4-3
Y46-26.2/Grt4-5
Y46-26.2/Grt4-6
Y46-26.2/Grt4-7
Y46-9.1/Grt4-1
Y46-9.1/Grt4-2
Y46-9.1/Grt4-3
Y46-9.1/Grt4-4
Y46-9.1/Grt4-5
Y46-9.1/Grt4-6
Y46-9.1/Grt4-7

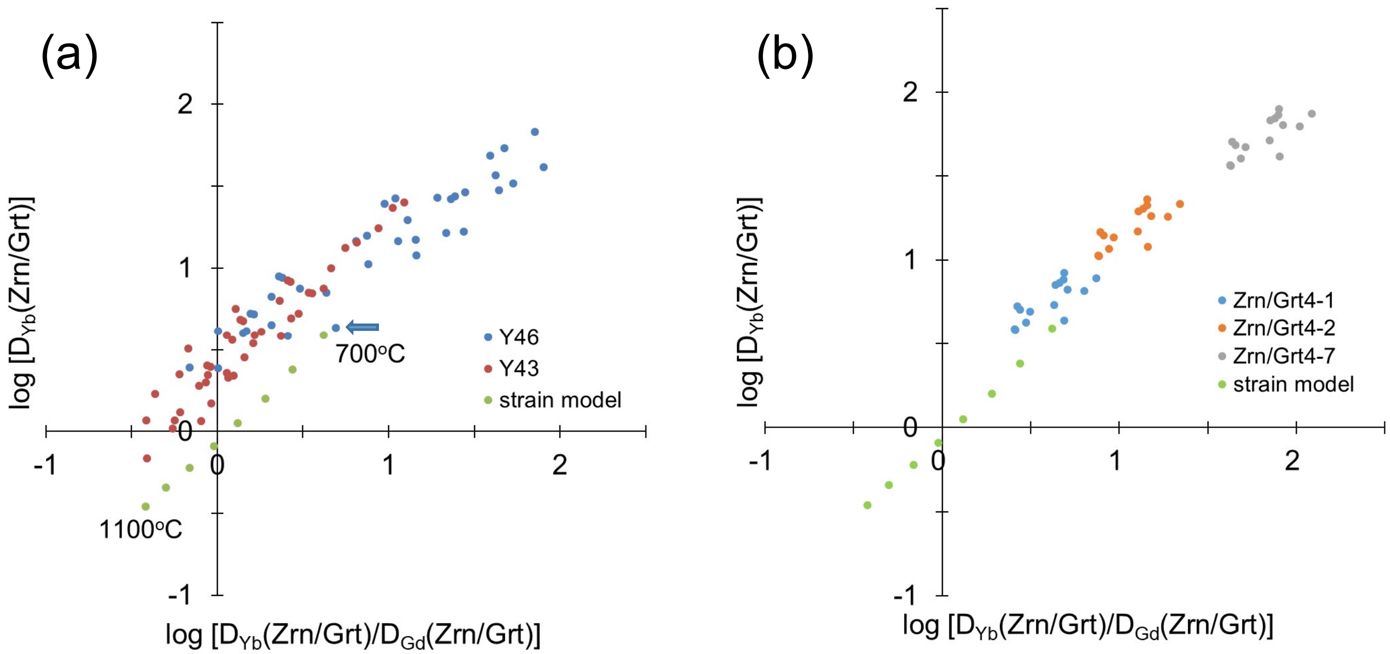
(a)
log [D_Yb(Zrn/Grt)]
log [D_Yb(Zrn/Grt)/D_Gd(Zrn/Grt)]
700°C
1100°C
Y46
Y43
strain model
-1
0
1
2
(b)
log [D_Yb(Zrn/Grt)]
log [D_Yb(Zrn/Grt)/D_Gd(Zrn/Grt)]
Zrn/Grt4-1
Zrn/Grt4-2
Zrn/Grt4-7
strain model
-1
0
1
2

Table s1. Analytical conditions for U–Pb zircon dating, trace elements (REE, Y, and Nb) including Hf, and Ti content of samples Y43 and Y46 by SHRIMP.

Target Elements		U–Pb		REE, Y, Nb, Hf	Ti
Sample Name		Y43	Y46	Y43, Y46	Y43, Y46
Grains with Rim Analyses / Total Analyzed Grains		23 / 33	10 / 42	44 / 44	44 / 44
Accepted Rim Analyses / Total Spots		29 / 72	16 / 64	44 / 44	44 / 44
Analytical Condition	beam diameter	~14 μm	~14 μm	~14 μm	~14 μm
	beam intensity	~0.96 nA	~0.96 nA	~0.70 nA	~0.77 nA
	mass resolution (M/ΔM at 1% of peak height)	~5200	~5200	~8600	~4000
	sensitivity (^{206}Pb ppm/nA)	~22	~22	~21	~21
Standards		TEMORA2[*1] (U-Pb calibration) 91500[*2] (U concentration)		91500[*8]	SL13[*9]
Secondary Standards		OD3 (33.0±0.1Ma[*3]): 33.0±0.3Ma (19 spots on 11 grain) SoriZ93 (93.9±0.6Ma[*4]): 94.0±0.8Ma (17 spots on 8 grain) OT4 (191.1±0.3[*5]): 190.4±1.9Ma (13 spots on 10 grain)			OT4 (6.8±3.1ppm[*5]): 6.4 ± 0.9ppm (SD) (5spots) TEMORA2 (10.2±7.3[*10] to 17±10 ppm[*11]): 9.7 ± 1.1ppm (SD) (10spots)
Age Calculation Method	data reduction	SQUID2[*6] and Isoplot3[*7]			
	weighted average	^{206}Pb/^{238}U age corrected by ^{207}Pb			
	initial Pb model	Stacey and Kramers (1975)			

[*1] Black et al. (2004), [*2] Wiedenbeck et al. (1995), [*3] Iwano et al. (2013), [*4] Ogasawara et al. (2013), [*5] Horie et al. (2013), [*6] Ludwig (2009), [*7] Ludwig (2012), [*8] Wiedenbeck et al. (2004), [*9] Hiess et al. (2008), [*10] Fu et al. (2008), [*11] Ickert et al. (2011).

SD=standard deviation

^{207}Pb correction was carried out assuming ^{206}Pb/^{238}U–^{207}Pb/^{235}U age-concordance.

References not cietd in the text

Black L.P., Kamo S.L., Allen C.M., Davis D.W., Aleinikoff J.N., Valley J.W., Mundil R., Campbell I.H., Korsch R.J., Williams I.S., Foudoulis C., 2004. Improved 206Pb/238U microprobe geochronology by the monitoring of a trace-element related matrix effect; SHRIMP, ID-TIMS, ELA-ICP-MS, and oxygen isotope documentation for a series of zircon standards. Chemical Geology 205, 115–140.
Fu, B., Page, Z., Cavosie, A.J., Fournelle, J., Kita, N.T., Lackey, J.S., Wilde, S.A., Valley, J.W., 2008, Ti-in-zircon thermometry: applications and limitations. Contribution to Mineralogy and Petrology, 156, 197-215.
Hiess, J., Nutman, A.P., Bennett, V.C., Holden, P., 2008, Ti-in-zircon thermometry applied to contrasting Archean metamorphic and igneous systems. Chemical Geology, 247, 323-338.
Ickert, R.B., Williams, I.S., Wyborn, D., 2011, Ti in zircon from the Boggy Plain zoned pluton: implications for zircon petrology and Hadean tectonics. Contributions to Mineralogy and Petrology, 162, 447-461.
Iwano H., Orihashi Y., Hirata T., Ogasawara, M., Danhara, T., Horie, K., Hasebe, N., Sueoka, S., Tamura, A., Hayasaka, Y., Katsube, A., Ito, H., Tani, K., Kimura, J.-I., Chang, Q., Kouchi, Y., Haruta, Y., Yamamoto, K., 2013. An interlaboratory evaluation of OD-3 zircon for use as a secondary U–Pb dating standard. Island Arc 22, 382–394.
Ogasawara M., Fukuyama M., Horie K., Sumii T., Takehara M., Sudo M., 2013. SHRIMP U–Pb age of SoriZ93 zircon from the Sori Granodiorite, Northeast Japan: A potential reference zircon of Late Cretaceous age. Island Arc 22, 306–317.
Stacey J.S., Kramers, J.D., 1975, Approximation of terrestrial lead isotope evolution by a two-stage model. Earth Planet Sci Lett, 26, 207–221.
Wiedenbeck M., Allé P., Corfu F., Griffin W.L., Meier M., Oberli F., von Quadt A., Roddick J.C., Spiegel W., 1995. Three natural zircon standards for U–Th–Pb, Lu–Hf, trace element and REE analyses. Geostandard Newsletter 19, 1–23.
Wiedenbeck, M., Hanchar, J.M., Peck, W.H., Sylvester, P., Valley, J., Whitehouse, M., Kronz, A., Morishita, Y., Nasdala, L., Fiebig, J., Franchi, I., Girard, J.-P., Greenwood, R.C., Hinton, R., Kita, N., Mason, P.R.D., Norman, M., Ogasawara, M., Piccoli., P.M. , Rhede, D., Satoh, H., Schulz-Dobrick, B., Skår, Ø., Spicuzza, M.J., Terada, K., Tindle, A., Togashi, S., Vennemann, T., Xie, Q. and Zheng, Y.-F., 2004. Further characterization of the 91500 zircon crystal. Geostandards and Geoanalytical Research 28, 9-39.

Table s2 (a) Summary of result of the SHRIMP U-Pb dating for sample Y43.

	Type	% $^{206}Pb_c$	U ppm	± ppm (2σ)	Th ppm	± ppm (2σ)	$^{206}Pb^*$ ppm	$^{232}Th/^{238}U$	$^{238}U/^{206}Pb^*$	±% (1σ)	$^{207}Pb^*/^{206}Pb^*$	±% (1σ)	Apparent age (Ma), ^{204}Pb correction: $^{206}Pb^*/^{238}U$ Age	Apparent age (Ma), ^{204}Pb correction: $^{207}Pb^*/^{206}Pb^*$ Age	Apparent age (Ma), ^{204}Pb correction: $^{208}Pb^*/^{232}Th$ Age	Apparent age (Ma), ^{207}Pb correction: $^{206}Pb^*/^{238}U$ Age
Y43-1.1	detrital core	0.14	330	9	170	6	8	0.531	33.759	1.9	0.04929	6.1	188 ±4	162 ±143	195 ±13	188 ±4
Y43-1.2	inner rim/inc	0.32	1157	21	6	1	14	0.005	69.992	2.0	0.04830	5.1	91.4 ±2	114 ±120	10.4 ±215	91.4 ±2
Y43-2.1	mixed (core/rim)	0.29	1223	45	57	10	39	0.048	27.071	1.2	0.05113	2.5	234 ±3	247 ±59	212 ±47	234 ±3
Y43-2.2	detrital core	0.70	193	7	150	6	74	0.804	2.232	2.4	0.15795	1.2	2386 ±47	2434 ±21	2419 ±75	2373 ±60
Y43-3.1	inner rim	0.27	714	15	5	0	9	0.007	72.033	3.0	0.04821	6.4	88.9 ±3	110 ±151	89.8 ±186	88.8 ±3
Y43-3.2	detrital core	0.31	412	11	147	5	114	0.368	3.102	1.6	0.11229	3.8	1801 ±25	1837 ±69	1832 ±51	1797 ±29
Y43-3.3	mixed (rim/rim/inc)	0.06	577	13	4	0	7	0.007	68.458	0.8	0.04699	2.7	93.5 ±0.7	48.7 ±64	107 ±78	93.6 ±0.8
Y43-4.1	mixed (rim/rim)	0.39	599	12	4	0	7	0.008	71.466	1.5	0.04873	7.7	89.6 ±1	135 ±180	21.3 ±209	89.5 ±1
Y43-4.2	detrital core	0.17	400	8	183	5	9	0.474	37.411	3.0	0.04970	5.1	170 ±5	181 ±120	163 ±11	170 ±5
Y43-4.3	inner rim	0.62	971	21	6	1	12	0.006	69.652	2.0	0.04771	7.2	91.9 ±2	85.0 ±172	97.4 ±321	91.9 ±2
Y43-5.1	mixed (core/rim)	0.16	1045	27	857	26	17	0.848	51.204	1.1	0.04977	3.9	125 ±1	184 ±92	128 ±4	124 ±1
Y43-5.2	detrital core	--	182	4	129	4	5	0.731	28.431	3.9	0.04948	7.0	223 ±9	171 ±164	243 ±18	223 ±9
Y43-5.3	mixed (rim/rim)	0.40	591	11	6	1	7	0.011	69.516	2.2	0.04921	6.7	92.1 ±2	158 ±157	119 ±125	91.9 ±2
Y43-6.1	detrital core	0.46	79	2	54	2	2	0.705	33.121	3.5	0.05048	13	192 ±7	217 ±298	163 ±21	192 ±7
Y43-6.2	inner rim	0.07	761	23	20	1	9	0.027	69.371	0.8	0.04687	10	92.3 0.7	42.4 ±246	105 ±45	92.4 0.9
Y43-7.1	detrital core	0.01	1402	42	817	26	33	0.602	36.765	1.8	0.04869	3.2	173 ±3	133 ±76	169 ±6	173 ±3
Y43-7.2	inner rim	0.12	873	18	5	0	11	0.006	69.182	0.7	0.04748	5.2	92.5 0.7	73.3 ±123	90.4 ±123	92.6 0.7
Y43-8.1	mixed (core/rim)	0.23	775	17	139	4	13	0.185	50.610	0.7	0.04936	4.5	126 0.9	165 ±105	128 ±10	126 1.0
Y43-8.2	mixed (rim/rim)	0.22	738	17	4	0	9	0.006	67.593	2.6	0.04818	6.0	94.7 ±2	108 ±141	113 ±214	94.6 ±2
Y43-9.1	detrital core	0.13	330	7	177	5	11	0.552	26.679	1.8	0.05059	5.3	237 ±4	222 ±121	251 ±14	237 ±4
Y43-9.2	inner rim	0.13	984	17	6	1	12	0.006	68.766	1.2	0.04778	5.0	93.1 ±1	88.3 ±118	94.0 ±140	93.1 ±1
Y43-10.1	detrital core	0.50	383	13	117	5	113	0.316	2.906	3.8	0.12073	0.5	1906 ±63	1967 ±9	1982 ±79	1898 ±72
Y43-10.2	inner rim	--	634	19	4	0	8	0.006	70.747	2.3	0.04760	6.0	90.5 ±2	79.5 ±141	91.6 ±18	90.5 ±2
Y43-11.1	Disc./detrital core	2.25	210	5	198	6	68	0.973	2.592	4.0	0.14762	7.6	2104 ±72	2319 ±131	1966 ±153	2062 ±87
Y43-12.1	detrital core	0.11	1117	27	1722	44	33	1.593	28.881	1.7	0.05141	2.6	219 ±4	259 ±60	215 ±6	219 ±4
Y43-13.1	Disc./detrital core	4.27	220	4	16	1	45	0.073	4.055	12.9	0.12328	12	1421 ±164	2004 ±214	1161 ±227	1367 ±171
Y43-13.2	Disc./detrital core	2.71	1057	29	66	4	141	0.064	6.276	8.4	0.09239	9.3	953 ±74	1475 ±176	227 ±47	929 ±76
Y43-13.3	Disc./detrital core	6.55	1201	28	59	7	77	0.051	12.530	8.9	0.10836	6.1	495 ±42	1772 ±111	211 ±53	464 ±40
Y43-14.1	mixed (rim/rim)	0.07	1080	35	70	3	14	0.067	68.503	1.1	0.04748	3.9	93.4 ±1	73.3 ±92	91.8 ±7	93.5 ±1
Y43-14.2	detrital core	0.42	145	4	105	4	4	0.748	33.332	2.7	0.04951	11	191 ±5	172 ±256	156 ±17	191 ±5
Y43-14.3	mixed (core/rim)	0.69	1394	39	200	6	30	0.148	40.063	1.6	0.04965	4.2	159 ±2	178 ±97	182 ±16	159 ±2
Y43-15.1	detrital core	--	111	3	62	3	32	0.575	3.004	3.1	0.11193	1.9	1852 ±49	1831 ±35	1863 ±140	1855 ±56
Y43-15.2	Disc./mixed (core/rim)	5.35	646	15	49	2	72	0.078	7.289	1.5	0.10948	2.5	829 ±12	1791 ±46	1230 ±54	787 ±12
Y43-16.1	mixed (core/mantle)	1.14	944	32	351	13	16	0.384	51.354	1.2	0.04861	3.9	124 ±1	129 ±93	124 ±7	124 ±1
Y43-16.2	mixed (rim/rim/inc)	0.43	960	20	49	2	12	0.052	67.995	1.2	0.04782	4.2	94.1 ±1	90.2 ±99	100 ±14	94.1 ±1
Y43-17.1	mantle	0.51	157	4	58	3	4	0.380	32.535	2.6	0.05051	7.5	195 ±5	218 ±174	195 ±25	195 ±5
Y43-17.2	detrital core	--	864	18	516	12	26	0.617	28.319	1.2	0.05021	1.5	224 ±3	205 ±35	223 ±8	224 ±3
Y43-17.3	inner rim	--	727	24	26	1	9	0.037	68.326	2.8	0.04693	5.3	93.7 ±3	45.6 ±126	92.8 ±14	93.8 ±3
Y43-18.1	detrital core	0.14	179	6	102	4	5	0.590	33.042	2.4	0.05027	7.9	192 ±4	208 ±184	196 ±16	192 ±5
Y43-18.3	mixed (rim/rim)	0.23	747	19	15	1	9	0.021	68.568	1.3	0.04811	6.1	93.3 ±1	105 ±144	95.9 ±61	93.3 ±1
Y43-19.1	inner rim	0.13	826	17	4	0	10	0.006	71.973	2.2	0.04755	5.4	89.0 ±2	76.8 ±128	94.6 ±117	89.0 ±2
Y43-19.2	detrital core	0.25	995	19	494	11	277	0.513	3.082	1.2	0.11261	0.7	1811 ±19	1842 ±12	1838 ±42	1808 ±22
Y43-19.3	mixed (core/rim)	3.14	1086	22	12	1	22	0.011	40.762	1.8	0.07344	2.9	156 ±3	1026 ±60	439 ±103	152 ±3
Y43-20.1	inner rim	0.39	912	20	7	1	11	0.008	70.079	2.4	0.04934	5.9	91.3 ±2	164 ±139	99.1 ±145	91.2 ±2
Y43-20.2	detrital core	0.11	691	18	236	7	234	0.353	2.532	1.4	0.13422	4.3	2146 ±25	2154 ±74	2150 ±37	2144 ±34
Y43-20.3	mixed (rim/rim/inc)	0.26	588	10	5	0	7	0.009	69.472	2.7	0.04788	7.1	92.1 ±2	93.1 ±169	93.2 ±182	92.1 ±3
Y43-21.1	detrital core	0.14	310	7	54	2	87	0.179	3.048	2.0	0.11294	2.0	1829 ±31	1847 ±35	1817 ±74	1827 ±35
Y43-22.1	detrital core	0.02	800	21	386	11	26	0.498	26.741	2.1	0.04983	3.5	237 ±5	187 ±81	230 ±18	237 ±5
Y43-22.2	mixed (rim/rim)	0.55	793	20	20	3	10	0.026	68.760	2.2	0.04876	6.6	93.1 ±2	136 ±155	87.1 ±53	93.0 ±2
Y43-23.1	inner rim	0.07	914	22	6	1	11	0.007	69.358	2.0	0.04717	5.5	92.3 ±2	58.0 ±132	102 ±82	92.4 ±2
Y43-23.2	detrital core	0.63	171	5	136	5	4	0.818	33.050	2.7	0.04771	12	192 ±5	84.8 ±278	203 ±18	193 ±5
Y43-23.3	inner rim	--	763	15	6	1	10	0.008	68.294	1.4	0.04750	5.5	93.7 ±1	74.7 ±130	182 ±71	93.8 ±1
Y43-24.1	mixed (rim/rim)	0.41	583	15	5	1	7	0.009	70.442	2.5	0.04851	5.0	90.9 ±2	124 ±117	107 ±147	90.8 ±2
Y43-24.2	mixed (core/rim)	0.20	1157	21	711	15	23	0.635	43.511	1.2	0.04977	5.9	146 ±2	184 ±139	146 ±5	146 ±2
Y43-25.1	mixed (core/rim)	1.29	925	19	42	2	18	0.046	44.478	6.4	0.05912	8.5	143 ±9	571 ±184	327 ±38	142 ±9
Y43-25.2	detrital core	--	374	11	132	5	108	0.366	2.997	1.8	0.11170	1.8	1856 ±30	1827 ±33	1805 ±73	1860 ±34
Y43-26.1	detrital core	--	836	23	574	17	25	0.709	28.991	1.3	0.05003	3.1	219 ±3	196 ±71	217 ±8	219 ±3
Y43-27.1	outer rim	--	412	7	2	0	5	0.006	69.975	3.0	0.04681	14	91.5 ±3	39.6 ±328	78.4 ±15	91.6 ±3
Y43-27.2	detrital core	--	2226	45	1135	25	58	0.527	33.318	1.0	0.04808	2.1	191 ±2	103 ±49	190 ±5	191 ±2
Y43-27.3	outer rim	0.64	438	14	4	0	5	0.010	70.783	1.8	0.04774	11	90.4 ±2	86.2 ±250	184 ±217	90.4 ±2
Y43-28.2	Disc./mantle	0.77	251	8	131	5	17	0.541	12.557	2.3	0.06609	4.3	494 ±11	809 ±89	603 ±33	489 ±11
Y43-28.3	detrital core	--	117	3	68	3	12	0.599	8.421	3.0	0.06319	4.2	723 ±21	715 ±89	723 ±30	724 ±21
Y43-28.4	mixed (rim/rim)	--	849	29	18	1	11	0.022	67.990	1.4	0.04627	5.1	94.1 ±1	11.9 ±122	93.6 ±23	94.3 ±1
Y43-29.1	inner rim	0.14	1009	19	12	1	12	0.012	72.149	3.2	0.04802	7.3	88.7 ±3	100 ±173	92.6 ±27	88.7 ±3
Y43-29.2	Disc./detrital core	3.41	846	31	39	2	184	0.048	3.825	6.8	0.12039	5.5	1497 ±91	1962 ±97	2400 ±296	1451 ±96
Y43-30.1	inner rim	0.05	1009	24	27	2	13	0.027	68.439	1.2	0.04825	4.8	93.5 ±1	112 ±112	91.3 ±17	93.5 ±1
Y43-30.2	detrital core	0.03	430	11	264	8	13	0.633	29.295	3.7	0.04986	2.9	216 ±8	189 ±67	235 ±14	217 ±8
Y43-31.1	detrital core	0.13	74	3	25	2	3	0.345	24.528	7.1	0.05063	12	258 ±18	224 ±286	265 ±41	258 ±18
Y43-32.1	detrital core	--	133	4	101	4	4	0.789	28.356	4.4	0.05028	14	223 ±10	208 ±336	196 ±19	224 ±10
Y43-33.1	outer rim/inc	0.09	556	18	5	1	7	0.010	70.714	3.0	0.04793	6.4	90.5 ±3	95.7 ±151	83.2 ±49	90.5 ±3
Y43-33.2	inner rim	0.02	1302	32	14	1	16	0.011	70.161	1.1	0.04759	3.8	91.2 ±1	79.2 ±91	97.2 ±22	91.3 ±1
Y43-33.3	detrital core	0.06	478	10	69	2	8	0.148	51.093	1.6	0.04898	5.9	125 ±2	147 ±138	126 ±15	125 ±2

Disc. = Discordant

Isotopic ratios are given with 1σ uncertainties, after the correction for common Pb using the ^{204}Pb correction method.

Pb_c and Pb^* indicate the common and radiogenic portions, respectively.

^{207}Pb correction was carried out assuming $^{206}Pb/^{238}U$–$^{207}Pb/^{235}U$ age-concordance.

Table s2 (b) Summary of result of the SHRIMP U-Pb dating for sample Y46.

													apparent age (Ma)			
													^{204}Pb correction			^{207}Pb correction
	Type	% $^{206}Pb_c$	U ppm	± ppm (2 σ)	Th ppm	± ppm (2 σ)	$^{206}Pb^*$ ppm	^{232}Th /^{238}U	^{238}U /$^{206}Pb^*$	±% (1 σ)	$^{207}Pb^*$ /$^{206}Pb^*$	±% (1 σ)	$^{206}Pb^*$ /^{238}U Age	$^{207}Pb^*$ /$^{206}Pb^*$ Age	$^{208}Pb^*$ /^{232}Th Age	$^{206}Pb^*$ /^{238}U Age
Y46-1.1	detrital core	0.05	416	9	211	6	9	0.525	40.880	0.9	0.04955	5.2	156 ±1	174 ±121	162 ±9	156 ±1
Y46-1.2	mixed (rim/rim)	0.02	896	18	44	3	11	0.051	69.595	3.3	0.04800	9.6	92.0 ±3	99.3 ±226	93.5 ±12	92.0 ±3
Y46-2.1	Disc detrital core	5.44	743	27	103	6	94	0.144	6.454	1.4	0.11218	1.3	929 ±12	1835 ±23	986 ±51	883 ±12
Y46-3.1	mixed (core/rim)	0.76	630	15	71	3	11	0.116	51.304	0.9	0.04823	7.3	124 ±1	110 ±173	147 ±46	124 ±1
Y46-3.2	detrital core	--	339	9	287	9	10	0.874	29.810	2.0	0.05015	4.9	213 ±4	202 ±114	229 ±11	213 ±4
Y46-4.1	Disc detrital core	4.66	76	3	20	1	14	0.270	4.501	4.4	0.11862	3.0	1293 ±52	1936 ±54	1522 ±170	1242 ±53
Y46-5.1	detrital core	0.71	528	12	222	6	237	0.434	1.897	1.6	0.19288	1.0	2730 ±35	2767 ±17	2748 ±82	2714 ±49
Y46-6.1	detrital core	0.17	967	20	290	7	21	0.310	39.544	1.3	0.04977	4.0	161 ±2	184 ±92	193 ±11	161 ±2
Y46-7.1	detrital core	--	861	21	452	13	26	0.542	28.775	2.2	0.05043	3.2	220 ±5	215 ±73	235 ±10	220 ±5
Y46-8.1	detrital core	0.02	292	7	51	3	83	0.182	3.041	3.5	0.11183	2.5	1833 ±56	1829 ±46	1801 ±108	1833 ±64
Y46-9.1	mixed (core/rim)	0.12	996	60	91	7	13	0.094	68.209	1.2	0.04764	4.9	93.8 ±1	81.3 ±116	101 ±19	93.9 ±1
Y46-9.2	detrital core	0.42	839	16	777	17	20	0.957	35.684	1.3	0.05021	5.0	178 ±2	205 ±116	174 ±7	178 ±2
Y46-9.3	mixed (core/rim)	0.12	582	13	45	3	7	0.080	69.293	1.5	0.04843	5.7	92.4 ±1	121 ±135	90.1 ±12	92.3 ±1
Y46-10.1	Disc detrital core	3.38	415	25	83	8	83	0.206	4.143	0.9	0.11527	1.2	1394 ±11	1884 ±21	1363 ±67	1351 ±12
Y46-11.1	inner rim	0.10	953	27	6	1	11	0.007	72.181	3.0	0.04781	5.4	88.7 ±3	89.8 ±127	37.6 ±86	88.7 ±3
Y46-11.2	mixed (core/rim)	0.01	966	25	253	10	19	0.271	44.655	2.1	0.04728	4.6	143 ±3	63.5 ±110	150 ±10	143 ±3
Y46-11.3	mixed (rim/rim)	0.24	735	20	4	0	9	0.006	68.569	1.4	0.04894	5.6	93.3 ±1	145 ±131	92.8 ±133	93.2 ±1
Y46-12.1	outer rim	0.08	706	15	6	1	9	0.008	71.301	1.4	0.04761	5.4	89.8 ±1	79.8 ±128	90.8 ±48	89.8 ±1
Y46-12.2	detrital core	0.99	447	11	292	8	10	0.673	37.637	1.7	0.04929	9.3	169 ±3	162 ±216	161 ±11	169 ±3
Y46-12.3	inner rim	0.14	851	17	8	1	11	0.010	67.857	2.4	0.04779	5.7	94.3 ±2	89.0 ±135	95.6 ±97	94.3 ±2
Y46-13.1	detrital rim	0.47	276	7	78	3	6	0.293	40.790	3.7	0.04873	8.2	156 ±6	135 ±193	166 ±29	156 ±6
Y46-13.2	Disc mixed (core/mantle)	6.48	403	10	182	6	25	0.465	12.783	3.6	0.10756	4.5	486 ±17	1758 ±83	216 ±16	456 ±16
Y46-14.1	detrital core	0.05	939	23	252	7	20	0.278	40.837	3.8	0.04775	4.8	156 ±6	86.9 ±113	129 ±12	156 ±6
Y46-14.2	Disc. mixed (mantle/mantle)	3.20	2356	72	2195	68	37	0.962	54.323	1.1	0.05501	11	118 ±1	413 ±245	95.3 ±6	117 1.0
Y46-15.1	detrital core	0.15	96	5	118	7	3	1.264	28.892	3.6	0.05168	9.9	219 ±8	271 ±226	248 ±20	219 ±8
Y46-16.1	detrital core	0.14	127	6	75	4	4	0.607	25.586	3.0	0.05228	7.8	247 ±7	298 ±179	273 ±25	247 ±8
Y46-17.1	detrital core	0.02	1614	28	391	8	38	0.250	36.099	1.8	0.04974	2.7	176 ±3	183 ±63	182 ±9	176 ±3
Y46-18.1	inner rim	0.25	932	36	14	1	11	0.015	70.291	1.3	0.04794	6.4	91.1 ±1	96.4 ±151	97.7 ±94	91.1 ±1
Y46-18.2	detrital core	0.04	176	6	48	2	4	0.282	40.526	6.3	0.04955	8.6	157 ±10	174 ±201	163 ±23	157 ±10
Y46-18.3	mixed (core/rim)	1.51	963	25	92	3	14	0.099	60.208	0.9	0.04589	12	106 1.0	-8 ±283	122 ±42	106 0.9
Y46-19.1	detrital core	--	131	4	77	3	5	0.608	24.859	3.0	0.04967	8.5	254 ±8	180 ±197	238 ±23	255 ±8
Y46-20.1	detrital core	0.24	1227	44	725	27	30	0.611	34.708	1.1	0.04998	6.2	183 ±2	194 ±144	198 ±7	183 ±2
Y46-21.1	mixed (rim/inc)	0.06	1058	35	72	3	13	0.071	68.820	0.7	0.04725	5.1	93.0 0.7	61.9 ±122	96.0 ±18	93.1 0.7
Y46-22.1	mixed (core/rim)	6.05	741	34	21	1	21	0.029	29.771	3.5	0.07715	7.3	213 ±7	1125 ±145		206 ±7
Y46-22.2	detrital core	--	116	7	68	5	46	0.607	2.158	1.7	0.15937	5.8	2455 ±35	2449 ±99	2423 ±271	2456 ±52
Y46-23.1	detrital core	0.25	524	15	290	9	12	0.572	38.401	0.9	0.04980	5.8	166 ±1	186 ±134	167 ±10	166 ±1
Y46-24.1	detrital core	--	238	7	166	6	6	0.721	32.034	2.3	0.04860	7.0	198 ±4	128 ±166	181 ±14	199 ±5
Y46-25.1	detrital core	0.07	1094	31	331	10	26	0.313	35.883	0.7	0.04799	4.6	177 ±1	99.0 ±108	177 ±7	178 ±1
Y46-26.1	inner rim	0.36	991	27	13	1	12	0.014	70.022	2.1	0.04784	6.6	91.4 ±2	91.4 ±157	94.6 ±114	91.4 ±2
Y46-26.2	mixed (rim/rim)	0.20	1046	41	34	2	13	0.034	66.985	2.2	0.04812	5.4	95.5 ±2	105 ±129	94.0 ±34	95.5 ±2
Y46-26.3	detrital core	0.64	542	16	267	9	17	0.510	28.011	3.6	0.05212	6.0	226 ±8	291 ±138	213 ±15	226 ±8
Y46-27.1	mixed (core/mantle)	4.54	709	17	26	1	42	0.038	13.878	5.9	0.09165	7.7	449 ±26	1460 ±146	596 ±123	429 ±25
Y46-27.2	Disc detrital core	7.64	335	12	36	2	31	0.111	8.506	4.6	0.12393	4.3	716 ±31	2014 ±76	782 ±70	665 ±30
Y46-28.1	inner rim	0.13	625	15	5	1	8	0.009	69.528	1.4	0.04807	5.7	92.1 ±1	103 ±135	89.8 ±73	92.0 ±1
Y46-28.2	detrital core	0.33	522	10	141	4	153	0.278	2.930	9.1	0.11799	6.5	1893 ±149	1926 ±116	1929 ±214	1888 ±170
Y46-29.1	detrital core	0.68	68	3	27	2	2	0.406	31.412	4.2	0.04975	14	202 ±8	183 ±333	211 ±32	202 ±8
Y46-30.1	detrital core	0.25	291	9	168	6	10	0.596	25.322	2.2	0.05148	6.0	250 ±5	262 ±138	221 ±16	250 ±5
Y46-31.1	detrital core	0.13	615	15	156	5	14	0.263	36.538	1.5	0.04932	5.1	174 ±3	163 ±120	192 ±14	174 ±3
Y46-32.1	mixed (core/mantle)	0.01	700	15	1054	25	21	1.555	28.962	2.4	0.04898	4.5	219 ±5	147 ±106	216 ±8	219 ±5
Y46-32.2	inner rim	--	689	13	37	2	9	0.055	68.249	1.4	0.04788	5.8	93.8 ±1	93.6 ±137	94.7 ±14	93.8 ±1
Y46-33.1	detrital core	0.23	178	5	109	4	13	0.630	12.204	2.7	0.05644	5.9	508 ±13	470 ±132	471 ±31	508 ±14
Y46-34.1	detrital core	0.18	3450	194	1243	72	82	0.372	36.021	3.9	0.05038	3.4	177 ±7	212 ±79	164 ±8	176 ±7
Y46-34.2	mixed (core/rim)	0.61	881	14	120	5	16	0.140	47.410	3.9	0.04885	6.9	135 ±5	141 ±161	136 ±23	135 ±5
Y46-35.1	detrital core	0.35	250	7	185	7	7	0.765	29.034	1.2	0.05061	8.6	218 ±3	223 ±199	224 ±15	218 ±3
Y46-36.1	detrital core	0.24	214	5	46	2	59	0.220	3.097	2.6	0.11210	3.5	1804 ±40	1834 ±64	1858 ±95	1800 ±46
Y46-37.1	detrital core	0.15	402	9	85	4	112	0.218	3.070	3.5	0.11218	4.1	1818 ±56	1835 ±74	1862 ±121	1815 ±63
Y46-38.1	outer rim	0.03	946	26	6	0	11	0.006	70.759	3.2	0.04723	6.5	90.5 ±3	60.8 ±154	88.6 ±103	90.5 ±3
Y46-38.2	inner rim	0.22	964	19	6	1	12	0.007	69.813	2.0	0.04799	6.2	91.7 ±2	98.6 ±146	91.0 ±180	91.7 ±2
Y46-38.3	detrital core	0.22	158	4	188	6	3	1.233	39.633	1.4	0.04809	8.0	161 ±2	104 ±188	160 ±13	161 ±2
Y46-38.4	inner rim	0.01	1136	28	8	1	14	0.007	69.400	2.2	0.04729	5.0	92.2 ±2	63.8 ±120	91.3 ±74	92.3 ±2
Y46-39.1	Disc detrital core	1.25	137	4	182	7	39	1.373	2.958	3.1	0.12309	1.9	1878 ±50	2001 ±34	1790 ±67	1860 ±56
Y46-40.1	detrital core	0.17	485	10	212	6	136	0.452	3.066	1.6	0.11224	1.1	1820 ±25	1836 ±20	1806 ±48	1818 ±28
Y46-41.1	detrital core	--	588	18	207	7	13	0.363	38.246	0.8	0.04846	4.6	166 ±1	122 ±107	172 ±12	167 ±1
Y46-42.1	detrital core	0.04	112	3	90	4	3	0.833	30.172	3.4	0.05064	10	210 ±7	224 ±238	215 ±20	210 ±7

Disc. = Discordant

Isotopic ratios are given with 1s uncertainties, after the correction for common Pb using the ^{204}Pb correction method.

Pb_c and Pb^* indicate the common and radiogenic portions, respectively.

^{207}Pb correction was carried out assuming ^{206}Pb/^{238}U–^{207}Pb/^{235}U age-concordance.

Table s2 (c) Concentrations of trace elements (REE, Y, and Nb) and Hf in zircon analyzed by SHRIMP.

sample Y43

	1.2	3.1	3.3	4.1	4.3	5.3	6.2	7.2	8.2	9.2	10.2	14.1	16.2	17.3	18.3
La (ppm)	0.043	0.093	0.059	0.065	0.091	0.14	0.15	0.030	0.15	0.064	0.091	0.073	0.10	0.046	0.20
Ce	0.20	0.31	0.24	0.26	0.33	0.46	0.46	0.15	0.42	0.22	0.27	0.32	0.43	0.19	0.63
Pr	0.044	0.052	0.054	0.060	0.070	0.084	0.091	0.048	0.080	0.047	0.049	0.059	0.091	0.044	0.11
Nd	0.24	0.30	0.36	0.39	0.51	0.73	0.78	0.32	0.50	0.30	0.29	0.35	0.77	0.33	0.58
Sm	0.42	0.37	0.37	0.46	0.49	0.57	0.62	0.43	0.49	0.42	0.27	0.37	0.83	0.58	0.47
Eu	0.060	0.056	0.052	0.052	0.061	0.085	0.11	0.055	0.060	0.064	0.040	0.061	0.11	0.065	0.093
Gd	4.5	4.0	3.5	4.5	4.8	4.4	4.7	4.8	5.1	4.9	3.0	4.7	5.2	4.7	4.0
Tb	3.8	3.1	2.9	3.7	3.8	3.3	4.2	3.8	4.3	4.1	2.4	3.1	3.4	4.7	3.0
Dy	68	55	51	64	69	59	58	70	76	71	47	55	58	68	51
Ho	34	29	26	32	35	30	27	36	38	36	24	29	29	31	26
Er	189	169	140	163	186	157	138	187	197	192	130	169	179	151	144
Tm	49	45	33	35	44	36	35	43	48	46	31	45	56	35	37
Yb	497	491	307	297	394	336	360	381	470	428	291	491	647	363	389
Lu	111	122	70	63	84	73	89	82	98	93	61	121	178	90	94
Y	1178	1033	918	1135	1228	1039	908	1231	1326	1244	845	1245	908	966	890
Nb	0.11	0.51	0.25	0.25	0.24	0.27	0.26	0.32	0.25	0.25	0.25	0.28	0.26	0.46	0.27
Hf	13389	13572	13660	13590	13498	13220	13087	13656	13158	13281	13681	13572	13087	13203	13003
Σ REE	958	919	635	662	823	701	717	807	937	875	589	919	1158	748	749
La/Gd	0.0017	0.019	0.014	0.012	0.016	0.026	0.027	0.0052	0.049	0.011	0.025	0.013	0.016	0.0082	0.043
La/Yb	0.000041	0.00013	0.00013	0.00015	0.00016	0.00028	0.00028	0.000053	0.00043	0.00010	0.00021	0.00010	0.00011	0.000086	0.00035
Gd/Yb	0.024	0.0066	0.0092	0.012	0.010	0.011	0.011	0.010	0.0088	0.0092	0.0085	0.0078	0.0065	0.011	0.0083
Ce/Ce*	0.97	1.06	0.95	0.91	0.95	1.01	0.94	0.79	0.64	0.91	0.97	1.12	1.00	0.91	1.01
Eu/Eu*	0.083	0.088	0.091	0.072	0.080	0.12	0.14	0.072	0.074	0.083	0.082	0.083	0.12	0.084	0.14
H/LREE	2009	1491	873	763	781	469	471	1262	843	1386	894	1362	913	1154	581
M/LREE	233	140	122	139	116	70	65	195	117	194	122	129	69	182	64
Σ LREE	0.33	0.44	0.47	0.52	0.67	0.95	1.03	0.40	0.73	0.41	0.43	0.48	0.96	0.42	0.90
Σ HREE	657	657	410	395	523	446	483	505	616	566	383	657	881	488	520

	19.1	20.1	20.3	22.2	23.1	23.3	24.1	27.1	27.3	28.4	29.1	30.1	33.1	33.2
La (ppm)	0.11	0.082	0.072	0.19	0.078	0.23	0.13	0.091	0.14	0.16	0.054	0.21	0.079	0.15
Ce	0.39	0.29	0.30	0.61	0.33	0.63	0.40	0.30	0.52	0.39	0.24	0.56	0.26	0.43
Pr	0.076	0.056	0.057	0.12	0.065	0.10	0.081	0.053	0.095	0.081	0.058	0.089	0.064	0.076
Nd	0.46	0.39	0.37	0.61	0.49	0.53	0.56	0.38	0.64	0.52	0.37	0.48	0.44	0.47
Sm	0.45	0.59	0.47	0.50	0.48	0.48	0.60	0.34	0.53	0.60	0.39	0.41	0.53	0.38
Eu	0.051	0.072	0.080	0.11	0.054	0.049	0.066	0.042	0.057	0.065	0.054	0.050	0.056	0.061
Gd	4.2	5.7	4.9	6.5	4.2	4.6	5.9	3.5	5.1	5.9	6.4	3.8	5.9	3.9
Tb	3.2	3.7	4.1	3.7	3.3	3.5	4.7	3.0	4.2	4.7	3.7	3.0	4.5	3.1
Dy	52	61	72	59	60	60	83	54	68	83	58	57	78	55
Ho	21	31	36	29	31	30	41	27	31	41	28	29	37	29
Er	80	174	190	159	167	158	207	138	140	203	156	159	179	159
Tm	16	43	42	39	41	39	44	30	28	44	41	38	37	40
Yb	118	432	368	400	374	378	375	250	226	373	439	367	305	408
Lu	24	97	78	92	83	84	79	53	46	78	105	82	62	96
Y	1032	1126	1257	1015	1085	1036	1440	947	1125	1855	997	1013	1331	987
Nb	0.25	0.25	0.27	0.24	0.35	0.32	0.29	0.25	0.24	0.30	0.30	0.38	0.27	0.29
Hf	13312	13409	13793	13388	13602	13317	13368	13224	13058	13233	13637	13640	13147	13931
Σ REE	320	849	797	791	765	759	842	560	550	836	838	740	710	796
La/Gd	0.022	0.012	0.012	0.025	0.016	0.042	0.019	0.022	0.022	0.022	0.0071	0.047	0.011	0.033
La/Yb	0.00064	0.00013	0.00013	0.00033	0.00014	0.00041	0.00024	0.00025	0.00041	0.00028	0.000084	0.00040	0.00018	0.00026
Gd/Yb	0.029	0.011	0.011	0.013	0.0090	0.010	0.013	0.011	0.018	0.013	0.012	0.0084	0.016	0.0078
Ce/Ce*	0.98	1.00	1.06	0.95	1.05	1.00	0.91	1.02	1.07	0.84	0.92	0.98	0.84	0.97
Eu/Eu*	0.074	0.079	0.10	0.11	0.080	0.066	0.069	0.074	0.069	0.069	0.055	0.082	0.060	0.10
H/LREE	245	1085	984	578	788	585	645	629	345	657	1207	625	687	775
M/LREE	92	134	163	76	107	79	122	115	89	124	140	82	151	88
Σ LREE	0.65	0.53	0.50	0.92	0.63	0.86	0.77	0.53	0.87	0.75	0.48	0.78	0.59	0.70
Σ HREE	158	572	489	532	498	501	498	333	300	496	585	487	404	545

sample Y46

	1.2	9.1	9.3	11.1	11.3	12.1	12.3	18.1	21.1	26.1	26.2	32.2	38.1	38.2	38.4
La (ppm)	0.13	0.21	0.14	0.029	0.032	0.16	0.049	0.066	0.076	0.11	0.11	0.083	0.10	0.072	0.045
Ce	0.45	0.52	0.43	0.16	0.17	0.53	0.25	0.28	0.27	0.31	0.41	0.30	0.26	0.29	0.22
Pr	0.074	0.10	0.095	0.038	0.040	0.11	0.058	0.069	0.046	0.060	0.088	0.060	0.044	0.065	0.048
Nd	0.38	0.56	0.56	0.26	0.33	0.65	0.35	0.57	0.36	0.42	0.57	0.40	0.30	0.41	0.35
Sm	0.48	0.53	0.47	0.40	0.33	0.54	0.44	0.54	0.42	0.48	0.46	0.38	0.36	0.38	0.48
Eu	0.065	0.057	0.049	0.055	0.049	0.090	0.078	0.069	0.072	0.068	0.076	0.076	0.077	0.080	0.057
Gd	5.4	5.2	5.1	4.3	3.0	4.9	3.6	6.9	5.9	5.5	5.6	6.3	5.5	4.5	3.6
Tb	4.1	4.2	4.2	3.7	3.1	4.4	3.4	4.8	5.4	3.9	4.8	3.3	4.5	4.2	4.1
Dy	67	68	68	67	57	75	58	75	83	70	77	51	76	75	69
Ho	31	31	31	34	28	35	29	35	41	34	35	24	36	38	35
Er	143	140	139	171	139	160	157	170	209	184	161	127	196	194	192
Tm	32	28	28	37	30	32	39	36	50	45	41	31	48	44	47
Yb	290	226	224	316	254	248	386	312	491	450	417	298	431	390	458
Lu	68	46	45	69	54	46	94	65	112	105	97	76	92	85	114
Y	1094	1125	1125	1192	1018	1297	1004	1255	1404	1168	1270	708	1266	1345	1237
Nb	0.28	0.25	0.25	0.29	0.28	0.32	0.31	0.30	0.26	0.30	0.32	0.30	0.26	0.26	0.26
Hf	13594	13058	13058	14164	13794	13533	13911	13583	13416	13998	13941	13137	13498	14241	13676
Σ REE	642	550	545	703	569	606	771	707	999	899	840	618	890	838	924
La/Gd	0.020	0.034	0.022	0.0057	0.0088	0.028	0.012	0.0081	0.011	0.016	0.017	0.011	0.015	0.013	0.011
La/Yb	0.00031	0.00063	0.00041	0.000063	0.000085	0.00045	0.000087	0.00014	0.00010	0.00016	0.00018	0.00019	0.00015	0.00013	0.000067
Gd/Yb	0.015	0.018	0.018	0.011	0.010	0.016	0.0075	0.018	0.0097	0.0098	0.011	0.017	0.010	0.0093	0.0064
Ce/Ce*	1.08	0.85	0.87	0.97	0.94	0.90	1.00	0.89	1.08	0.94	0.94	0.99	0.97	0.93	1.00
Eu/Eu*	0.076	0.069	0.061	0.080	0.10	0.11	0.13	0.064	0.078	0.079	0.086	0.078	0.091	0.11	0.10
H/LREE	668	342	375	1281	834	352	1148	587	1359	1017	718	749	1303	952	1390
M/LREE	132	88	97	228	154	92	144	123	196	134	113	112	196	154	173
Σ LREE	0.58	0.88	0.79	0.33	0.41	0.92	0.45	0.70	0.48	0.59	0.77	0.54	0.44	0.55	0.45
Σ HREE	389	300	297	423	339	325	519	413	653	600	555	405	571	520	619

Analytical errors of 80% for La; 30% for Pr, Nd, Gd, and Nb; 20% for Eu and Tb; and less than 15% for other REE. Most errors were derived from the reference concentration of 91500 (Wiedenbeck et al., 2004).

Ce* was calculated from C1-chondrite-normalized La and Pr on the basis of the following definition: Ce* = $(La/Pr)_{CN}/2$.

Eu* was calculated from C1-chondrite-normalized Sm and Gd on the basis of the following definition: Eu* = $(Sm/Gd)_{CN}/2$.

H/LREE represents the fractionation between HREE and LREE as estimated from La + Pr + Nd for LREE and Tm + Yb + Lu for HREE.

M/LREE represents the fractionation between MREE and LREE as estimated from La + Pr + Nd for LREE and Gd + Tb + Dy for MREE.

Table s2(d) Ti contents of zircon.

analysis number	Ti (ppm)	+/-	Watson et al. (2006) Ti-in-Zrn thermometry (°C) lowest	highest	Ferry & Watson (2007) (°C) highest	lowest	Activities assumed in Ferry & Watson (2007) aSiO2	aTiO2
Y43-1.2	1.30	0.05	598	579	662	603	1	0.5
Y43-4.1	1.66	0.07	614	595	682	620	1	0.5
Y43-3.1	1.23	0.04	594	575	658	599	1	0.5
Y43-3.3	1.97	0.06	626	606	696	634	1	0.5
Y43-4.3	1.63	0.06	613	593	680	619	1	0.5
Y43-5.3	2.12	0.09	631	611	702	638	1	0.5
Y43-6.2	1.85	0.06	622	602	691	629	1	0.5
Y43-7.2	1.80	0.05	620	600	688	627	1	0.5
Y43-8.2	1.43	0.05	604	585	670	609	1	0.5
Y43-9.2	1.39	0.04	602	583	667	608	1	0.5
Y43-10.2	1.66	0.05	614	595	682	621	1	0.5
Y43-14.1	1.81	0.06	620	600	689	627	1	0.5
Y43-16.2	1.94	0.10	625	605	694	631	1	0.5
Y43-17.3	1.32	0.05	599	580	664	604	1	0.5
Y43-18.3	1.50	0.05	607	588	673	613	1	0.5
Y43-19.1	1.93	0.07	624	604	694	631	1	0.5
Y43-20.1	1.26	0.06	596	577	660	599	1	0.5
Y43-20.3	1.43	0.05	604	585	670	609	1	0.5
Y43-22.2	1.67	0.07	614	595	682	620	1	0.5
Y43-23.1	1.90	0.07	623	603	693	630	1	0.5
Y43-23.3	1.39	0.05	602	583	667	607	1	0.5
Y43-24.1	1.97	0.07	626	606	696	633	1	0.5
Y43-27.1	1.32	0.05	599	580	664	603	1	0.5
Y43-27.3	1.97	0.08	626	606	696	633	1	0.5
Y43-28.4	1.90	0.08	623	604	693	630	1	0.5
Y43-29.1	1.81	0.07	620	600	689	626	1	0.5
Y43-30.1	1.51	0.05	608	588	674	613	1	0.5
Y43-33.1	1.47	0.06	606	587	672	611	1	0.5
Y43-33.2	1.69	0.10	615	596	683	620	1	0.5
Y46-1.2	1.81	0.06	620	601	689	627	1	0.5
Y46-9.1	1.82	0.09	620	601	689	626	1	0.5
Y46-9.3	2.04	0.10	628	608	698	634	1	0.5
Y46-11.1	1.47	0.05	606	587	672	612	1	0.5
Y46-11.3	1.56	0.05	610	591	677	616	1	0.5
Y46-12.1	1.52	0.05	609	589	675	614	1	0.5
Y46-12.3	1.90	0.06	623	603	693	630	1	0.5
Y46-18.1	1.64	0.05	613	594	681	619	1	0.5
Y46-21.1	1.76	0.05	618	598	686	625	1	0.5
Y46-26.1	2.19	0.09	633	613	705	641	1	0.5
Y46-26.2	2.25	0.07	635	615	707	643	1	0.5
Y46-32.2	2.22	0.08	634	614	706	642	1	0.5
Y46-38.1	1.63	0.05	613	594	680	619	1	0.5
Y46-38.2	1.66	0.08	614	595	682	619	1	0.5
Y46-38.4	1.38	0.05	602	583	667	607	1	0.5

Table s3 Representative REE and trace element analyses of garnet by LA-ICPMS.

analysis number	Y43Grt1-1	error (2SE)	Y43Grt1-2	error (2SE)	Y43Grt1-3	error (2SE)	Y43Grt1-4	error (2SE)	Y43Grt1-5	error (2SE)	Y43Grt1-6	error (2SE)	Y46Grt1-1	error (2SE)	Y46Grt1-2	error (2SE)
La (ppm)	b.d.		b.d.		b.d.		b.d.		b.d.		b.d.		b.d.		b.d.	
Ce	b.d.		b.d.		b.d.		b.d.		b.d.		b.d.		b.d.		b.d.	
Pr	b.d.		b.d.		b.d.		b.d.		b.d.		b.d.		b.d.		b.d.	
Nd	b.d.		b.d.		b.d.		b.d.		b.d.		b.d.		0.0560	0.0780	b.d.	
Sm	0.14	0.13	b.d.		0.04	0.08	0.12	0.13	0.21	0.18	0.27	0.20	0.16	0.14	0.30	0.17
Eu	b.d.		0.074	0.043	0.033	0.032	0.047	0.040	0.098	0.053	b.d.		0.038	0.032	0.017	0.023
Gd	2.2	0.5	2.9	0.6	2.4	0.6	2.6	0.7	1.1	0.4	2.4	0.5	1.7	0.4	2.7	0.6
Tb	1.3	0.1	2.2	0.2	1.8	0.2	1.6	0.2	1.0	0.1	1.6	0.2	1.1	0.2	1.8	0.2
Dy	21.1	1.4	37.0	1.4	34.9	1.8	27.8	1.6	19.6	1.4	22.6	1.8	17.8	1.4	26.0	1.6
Ho	9.8	0.5	15.7	0.7	17.6	0.6	12.3	0.5	8.9	0.4	8.2	0.5	6.2	0.4	10.5	0.5
Er	52.0	2.3	68.9	2.3	91.0	4.3	54.8	2.7	43.7	2.4	26.4	1.3	17.8	1.1	42.1	1.9
Tm	11.4	0.5	12.8	0.6	20.4	0.7	10.1	0.5	8.8	0.4	4.4	0.3	2.0	0.2	7.2	0.4
Yb	113.3	4.2	102.7	5.1	172.9	6.6	79.9	4.0	70.1	2.9	22.5	1.7	7.7	0.7	52.5	2.1
Lu	19.1	0.9	15.4	0.6	31.6	1.3	10.9	0.4	10.5	0.5	2.3	0.3	0.7	0.1	7.9	0.4
Y	253.0	9.6	318.0	10.0	328.7	8.8	266.1	8.2	238.4	6.6	233.4	6.2	167.7	6.5	226.3	7.1
Ti	26.6	5.6	28.9	6.2	29.1	6.6	24.5	4.8	28.1	6.5	21.0	5.9	29.7	4.2	23.1	4.4
Th	b.d.		b.d.		b.d.		b.d.		b.d.		b.d.		b.d.		b.d.	
U	b.d.		0.010	0.010	b.d.		0.010	0.010	b.d.		0.015	0.013	b.d.		0.013	0.010
P	73.0	17.0	134.0	14.0	77.0	12.0	120.0	16.0	144.0	21.0	190.0	17.0	150.0	17.0	84.0	13.0
Zr	1.7	0.3	6.8	0.9	4.4	0.7	3.5	0.7	2.6	0.5	7.2	1.2	3.0	0.5	4.3	0.6

analysis number	Y46Grt1-3	error (2SE)	Y46Grt1-4	error (2SE)	Y46Grt1-5	error (2SE)	Y46Grt1-6	error (2SE)	Y46Grt1-7	error (2SE)	Y46Grt1-8	error (2SE)	Y46Grt1-9	error (2SE)	Y46Grt4-1	error (2SE)
La (ppm)	b.d.		b.d.		b.d.		b.d.		0.021		b.d.		b.d.		b.d.	
Ce	b.d.		b.d.		0.011	0.015	b.d.		0.047	0.025	0.036	0.023	0.043	0.032	b.d.	
Pr	b.d.		b.d.		b.d.		b.d.		0.012	0.014	b.d.		b.d.		b.d.	
Nd	b.d.		b.d.		b.d.		b.d.		0.055	0.076	b.d.		b.d.		0.031	0.062
Sm	0.26	0.17	0.25	0.17	0.15	0.14	0.30	0.18	0.19	0.15	0.03	0.06	b.d.		0.26	0.18
Eu	0.074	0.043	b.d.		0.068	0.043	0.018	0.025	0.023	0.026	0.007	0.015	0.024	0.027	b.d.	
Gd	4.3	0.7	4.9	0.8	6.5	1.0	4.5	0.7	3.9	0.6	2.1	0.5	1.9	0.5	3.5	0.6
Tb	3.1	0.2	4.3	0.3	5.0	0.4	4.1	0.3	3.6	0.3	2.5	0.2	2.2	0.2	1.8	0.2
Dy	39.9	1.9	48.3	2.5	69.1	2.0	74.8	3.1	74.5	3.0	53.2	2.1	51.3	2.0	24.8	1.5
Ho	11.6	0.7	12.6	0.5	20.2	0.7	33.8	1.2	34.5	1.3	27.6	1.2	27.0	0.9	8.6	0.5
Er	39.3	2.1	39.0	2.1	63.6	2.6	151.8	4.4	171.8	5.5	143.9	5.8	139.7	4.6	35.1	1.8
Tm	6.3	0.5	6.1	0.4	11.4	0.4	35.1	1.1	38.9	1.3	33.6	1.1	33.8	1.2	7.1	0.4
Yb	45.2	2.4	44.8	2.3	89.7	3.6	316.0	10.0	353.0	10.0	330.0	12.0	306.6	8.5	58.8	3.3
Lu	6.4	0.3	5.6	0.5	11.0	0.5	50.6	1.9	54.9	2.1	52.0	1.5	49.6	1.6	8.9	0.5
Y	319.6	9.4	361.0	11.0	551.0	18.0	801.0	21.0	847.0	28.0	695.0	19.0	640.0	21.0	240.8	7.3
Ti	34.4	5.3	59.8	9.5	131.0	31.0	170.0	44.0	53.5	8.6	105.0	25.0	450.0	150.0	25.2	5.8
Th	b.d.		b.d.		0.017	0.020	0.016	0.018	0.12	0.05	0.12	0.05	0.031	0.024	b.d.	
U	0.012	0.010	b.d.		0.021	0.019	0.0094	0.0090	0.023	0.012	0.037	0.020	0.042	0.018	b.d.	
P	94.0	13.0	70.0	13.0	69.0	14.0	36.7	8.6	35.0	13.0	39.0	11.0	28.0	12.0	116.0	16.0
Zr	3.5	0.4	2.8	0.5	3.2	0.5	1.3	0.3	1.1	0.3	1.6	0.6	1.0	0.3	4.4	0.6

analysis number	Y46Grt4-2	error (2SE)	Y46Grt4-3	error (2SE)	Y46Grt4-4	error (2SE)	Y46Grt4-5	error (2SE)	Y46Grt4-6	error (2SE)	Y46Grt4-7	error (2SE)
La (ppm)	b.d.		b.d.		b.d.		b.d.		b.d.		0.016	0.022
Ce	b.d.		0.011	0.015	b.d.		b.d.		b.d.		0.042	0.025
Pr	b.d.		b.d.		b.d.		b.d.		b.d.		b.d.	
Nd	0.21	0.14	b.d.		b.d.		b.d.		b.d.		0.081	0.091
Sm	0.37	0.20	0.35	0.20	0.62	0.25	0.40	0.20	0.30	0.18	0.77	0.34
Eu	0.018	0.026	0.037	0.035	0.065	0.041	b.d.		b.d.		0.024	0.027
Gd	3.7	0.7	4.0	0.9	4.5	0.8	4.9	1.0	5.0	0.8	5.9	0.9
Tb	1.9	0.2	2.2	0.2	2.3	0.2	2.3	0.2	2.2	0.2	2.4	0.2
Dy	24.4	1.4	24.3	1.4	23.7	1.4	24.3	1.5	23.9	1.7	25.5	1.6
Ho	6.3	0.4	5.7	0.4	5.4	0.4	5.0	0.3	5.2	0.4	4.8	0.4
Er	19.3	1.2	16.4	1.1	12.2	0.9	11.6	1.0	13.7	1.0	9.1	0.5
Tm	3.1	0.2	2.6	0.2	1.5	0.2	1.4	0.2	2.2	0.2	1.2	0.1
Yb	21.3	1.5	15.5	1.2	8.5	0.7	7.7	0.7	15.2	1.1	6.1	0.6
Lu	2.9	0.3	1.9	0.2	1.1	0.2	0.8	0.1	2.0	0.2	0.5	0.1
Y	181.9	6.1	162.9	4.6	150.4	4.8	148.1	5.5	151.2	4.4	141.9	4.9
Ti	26.6	5.8	33.0	5.6	46.3	8.4	40.8	5.4	30.9	6.2	25.3	5.0
Th	b.d.		b.d.		b.d.		0.037	0.026	b.d.		0.031	0.024
U	0.017	0.012	b.d.		b.d.		b.d.		0.015	0.010	0.015	0.011
P	150.0	13.0	162.0	13.0	164.0	14.0	148.0	13.0	142.0	15.0	107.0	12.0
Zr	7.5	0.9	7.9	1.1	7.2	0.9	7.8	0.8	8.0	0.7	5.2	0.7

b.d.: below detection limit.